Master of Science Thesis

Continuous correction function for the influence of gaps and overlaps for the optimization of curved variable stiffness laminates

F.J. van Zanten

Faculty of Aerospace Engineering · Delft University of Technology

Continuous correction function for the influence of gaps and overlaps for the optimization of curved variable stiffness laminates

Master of Science Thesis

For obtaining the degree of Master of Science in Aerospace Engineering
at Delft University of Technology

F.J. van Zanten

27th of August 2018

Faculty of Aerospace Engineering · Delft University of Technology

The work in this thesis was supported by GKN Aerospace. Their cooperation is gratefully acknowledged.

Delft University of Technology
Faculty of Aerospace Engineering
Department of Aerospace Structures and Materials

GRADUATION COMMITTEE

Dated: 27th of August 2018

Chair holder: Dr.ir. R. de Breuker

Committee members:

Dr.ir M. van Tooren

Dr.ir. S. Koussios

Dr.ir. O.K. Bergsma

Abstract

In this manuscript an approach for the optimization for strength of curved variable stiffness laminates is proposed. A correction function to estimate the effect of gaps and overlaps based on the design variables is evaluated. To allow the currently available multiple mesh optimization approach (MMOA) to be applied to curved surfaces, the method is adapted. A secondary coarse mesh is defined and in the nodes of this mesh the fibre angles are defined. The elements of the secondary mesh are rotated into a plane and inverse isoparameticly mapped the centroids of the finite element (FE) mesh in these elements are found. The fibre angles are interpolated in these centroids and exported to ABAQUS® for an evaluation of the stress field. To find a density correction function initially an approximation function is defined, in the process of evaluating the correction function complications regarding the boundary conditions are encountered. These are generated by 'shockwaves' that occur during the lay-up processing depending on the manufacturing strategy, a FE solution proposed and evaluated.

Table of Contents

List of Figures

List of Tables

Preface

In this thesis some of the research I performed under Dr. van Tooren for GKN Aerospace some of this research is published in the papers:

"F.J. van Zanten, C. Pupo, D. Barazanchy, M. van Tooren. Fiber angle optimization and tow path planning on 3D curved surfaces using the multiple mesh approach. ASC 33rd Annual Technical Conference. September 2018 Seattle (USA)"

In addition to the work done for this paper, this master thesis discusses finding a correction factor for the stiffness of variable stiffness laminates based on discrete fibre angles.

I would like to thank my supervisor Dr.ir M. van Tooren for his assistance during the writing of this thesis, the discussions and the suggestions provided were always of great value. I am grateful for the suggestions provided to me by Dr. D. Barazanchy. I would like to express my appreciation to Chris Sacco for the fruitful mathematical and programming discussions, and Fokker for providing funds in a research subject related to this thesis. Finally I'd like to thank Dr.ir. S. Koussios for the extended feedback on the thesis work.

Delft, University of Technology
27th of August 2018

F.J. van Zanten

List of Abbrevations

List of Acronyms

AFP	automated fibre placement
CLPT	classical laminated plate theory
CM	calculation mesh
CS	constant stiffness
FE	finite element
FEA	finite element analysis
FEM	finite element method
GUI	graphical user interface
KLPT	Kirchoff-Love plate theory
LPA	lamination parameter approach
MM	manufacturing mesh
MMOA	multiple mesh optimization approach
RBF	radial basis functions
NURBS	non-uniform rational basis spline
VS	variable stiffness

“Imagination is more important than knowledge. Knowledge is limited. Imagination encircles the world.”

— *Albert Einstein*

Chapter 1

Introduction

The introduction of new technologies like automated fibre placement (AFP) allows for the creation of variable stiffness (VS) laminates. These laminates can be tailored to their loading condition by varying the fibre angle in the ply, whereas constant stiffness (CS) laminates have the same fibre angle throughout the ply. VS laminates have been discussed extensively by B.F. Tatting [7], S. Setoodeh [8] and M. van Tooren [9]. In this literature two main approaches are identified. The first uses the lamination parameters, as defined by Hahn and Tsai [10], as design variables; this is a stiffness based approach. In order to reduce the design variables, the second approach meshes the geometry with a rough mesh in which the fibre angles in the nodes are the design variables. The design variables are then interpolated onto a normal finite element method (FEM) which is evaluated to acquire the stress field. Van Tooren et al. [6] discusses an approach to find a continuous correction function for the gaps and overlaps caused by fibre steering.

In this manuscript the goal is to create a methodology that allows for the optimization of curved VS laminates. The methodologies discussed above are capable of optimizing VS laminates on flat plates, however this process has not been reported on before for curved surfaces. A possible solution for the density function was presented in [6], however this solution is only capable of taking in account the gaps and overlaps in flat laminates.

The workflow of this process is shown in Figure 3.1. These methodologies are limited to 2D shells, a methodology to extend one of these approaches such that it can be used on 3D shells is discussed in Chapter 3.

During the design of VS laminates gaps and overlaps are created; ideally these should be taken in account during the optimization process. To achieve this Van Tooren et al. [6] used a function to approximate the change in density over the surface as a function of the discrete fibre angles. The process of finding this function for 2D surfaces is discussed in section 6.1, to move this process to a 3D surface; the same approach as proposed for the optimization process in Chapter 3 is valid. During the course of this thesis complications are found and a solution is presented in section 6.2.

Chapter 2

Literature Review

2.1 What approach for optimizing the fibre paths in a fibre steered laminate will lend itself the best for the purpose of the research?

To optimize the strength using the fibre orientation of a fibre steered plate, multiple methods are available in the literature. To take the fibre orientation in each Finite Element (FE) mesh element for each ply would cause the optimization problem to have an overwhelming amount of design variables, which would result in time costly optimization problem. To reduce the design variables two optimization approaches are available in the literature. The first method discussed is to optimize panels for stiffness through the usage of Laminate Parameters (LP). The other approach is to use a secondary mesh, called the Manufacturing Mesh (MM) which is laid over the mesh the FE solver uses. On the nodes of this coarser mesh the fibre angles are the design variables, then through a mapping and interpolation process the fibre angles in the FE mesh are found.

2.1.1 Laminate parameter approach

To reduce the amount of design variables for the optimizer, the laminate configuration can be expressed as the laminate parameters, as demonstrated by Tsai and Hahn [10]. The geometric lamination parameters as a function of the fibre angle are shown in the following equation:

$$
\begin{aligned}
[V_{1A}, V_{1B}, V_{1D}] &= \int_{-1/2}^{1/2} \cos 2\theta \left[1, z, z^2\right] dz \\
[V_{2A}, V_{2B}, V_{2D}] &= \int_{-1/2}^{1/2} \cos 4\theta \left[1, z, z^2\right] dz \\
[V_{3A}, V_{3B}, V_{3D}] &= \int_{-1/2}^{1/2} \sin 2\theta \left[1, z, z^2\right] dz \\
[V_{4A}, V_{4B}, V_{4D}] &= \int_{-1/2}^{1/2} \sin 4\theta \left[1, z, z^2\right] dz
\end{aligned}
\tag{2.1}
$$

By isolating the lamination parameters from the material invariants found by Tsai and Pagano [11], Tsai and Hahn then related the lamination parameters to the in-plane stiffness matrix. This was then expanded upon by finding formulations for the coupling and bending stiffness matrices as shown in equation 2.2. Based on these formulas Miki [12] established a new and unified optimal design method for composite laminates. This approach assumes that the laminated plates are symmetric. This design method reduces the number of variables of the optimization problem to 12 lamination parameters, 4 per stiffness matrix. However this simplification brings consequences, the first of which is that the lamination parameters are found through the usage of the Classical Laminate Theory (CLT) this implies that the laminate is assumed to be thin thus the out of plane stresses and transverse shear stresses are neglected in the problem. The CLT assumes perfect bonding, therefore the interlaminar stresses are assumed to be zero.

$$
\begin{aligned}
[A_{11}, B_{11}, D_{11}] &= U_1 \left[h, 0, \frac{h^3}{12}\right] + U_2 \left[V_{1A}, V_{1B}, V_{1D}\right] + U_3 \left[V_{2A}, V_{2B}, V_{2D}\right] \\
[A_{22}, B_{22}, D_{22}] &= U_1 \left[h, 0, \frac{h^3}{12}\right] - U_2 \left[V_{1A}, V_{1B}, V_{1D}\right] + U_3 \left[V_{2A}, V_{2B}, V_{2D}\right] \\
[A_{12}, B_{12}, D_{12}] &= U_4 \left[h, 0, \frac{h^3}{12}\right] - U_3 \left[V_{2A}, V_{2B}, V_{2D}\right] \\
[A_{66}, B_{66}, D_{66}] &= U_5 \left[h, 0, \frac{h^3}{12}\right] - U_3 \left[V_{2A}, V_{2B}, V_{2D}\right] \\
[A_{16}, B_{16}, D_{16}] &= \frac{U_2}{2} \left[V_{3A}, V_{3B}, V_{3D}\right] + U_3[V_{4A}, V_{4B}, V_{4D}] \\
[A_{26}, B_{26}, D_{26}] &= \frac{U_2}{2} \left[V_{3A}, V_{3B}, V_{3D}\right] - U_3[V_{4A}, V_{4B}, V_{4D}]
\end{aligned}
\tag{2.2}
$$

The optimization problem is not necessarily convex. The optimal lamination parameters return a stiffness matrix. An infinite number of different lay-ups can result in this stiffness matrix. To solve for the fibre angles genetic algorithm or search techniques are used, however these are computationally inefficient at finding a global optimum. Foldager et al. [13] proposed a method using the strain energy to create convexity in the problem of finding the ply angles and thicknesses.

Failure criteria evaluate whether a laminate has failed; Through the ply strain the ply stresses are found using the ABD matrix. The ply strains are a function of the laminate strain and the ply angle. This poses a problem since in the lamination parameter approach the ply angles are undefined. To solve this problem, IJsselmuiden [14] developed a method to find the area in the strain space that is safe to be designed within. This was done by mapping the Tsai-Wu failure criterion in the strain space. This space is limited by the worst case fibre angle. As such the failure criterion provides a conservative approximation of the Tsai-Wu failure criterion. The approach implies that all possible ply angles could be at all possible locations in the laminate, significantly reducing the design space. Khani [15] elaborates on the method developed by IJsselmuiden, by using a hybrid approximation for the failure index. This was improved upon by Peeters et al. [16] by taking in account the size of a tow, and the maximum size of a gap or overlap created by the fibre paths during the post-processing. During the optimization these defects are not taken into account.

The lamination parameter approach allows for the design variables to be reduced to just 12 per finite element (FE) element, however it also inhibits the design tool to view the fibre angles during optimization and thus the gaps and overlaps can not be taken in account during the optimization process. This form of optimization is also limited by the assumptions made in the CLT.

2.1.2 Multiple Mesh Approach

The multiple mesh optimization approach (MMOA) differs from the lamination parameter approach (LPA) as it does not remove the ply angles from the optimization problem. Instead it employs a secondary coarser mesh named the manufacturing mesh (MM) as explained by van Tooren [9] and places this mesh over the mesh used for finite element analysis (FEA). The mesh used during the FEA is referred to as the calculation mesh (CM). In the nodes of the MM fibre angles are defined, and these are the design variables used by the optimization algorithm to find a solution.

By interpolating the fibre angles of the MM element nodes to the centroids of the elements in the CM, the amount of design variables can be reduced. This concept is shown in figure 2.1. The smoothness of the fibre paths over the mesh element boundaries is guaranteed [4], however the change in fibre angle is not continuous as the solution is using Lagrangian interpolation functions which are not C^1 continuous.

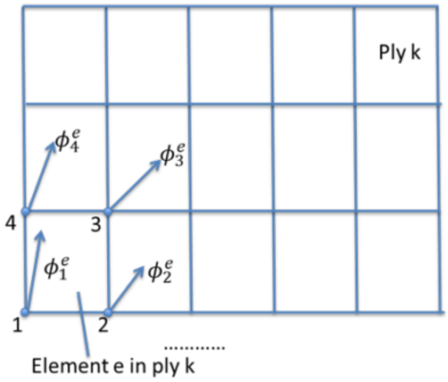

Figure 2.1: The manufacturing mesh with the fibre angles in the nodes. [1]

The reduction in design variables depends on the coarseness of the MM. The coarser the MM, the fewer design variables, however this also reduces how close the solution can approach the true optimal solution. For simple load cases with simple geometries this phenomenon plays a less significant role. As the geometry starts incorporating holes and other complexities this could become an issue. The usage of a secondary mesh allows for the manufacturing constraints such as the minimum turn radius to be applied easily by constraining the change in fibre angle. This method however, does rapidly increase in the number of design variables as layers are added to the composite layup, while the previously discussed lamination property approach does not.

The solution approach presented by van Tooren et al. [9] was used by Barazanchy [1] on various load cases, in this article a solution is found for the load case of: Pure tensile, pure shear, pure compression loading, and a plate with a hole loaded under pure tension. To find a solution, a global search algorithm based on the basin of attraction was used. To avoid finding local minima, different initial laminates were used for each of the load cases. The solution is compared to solution created by the LPA, and the results of the MMOA match the expected results based on literature.

An issue discussed in [4] is the smoothness of the density function across the element boundaries. A possible solution could be through implementing the Hermite interpolation function. An area of concern that is remarked upon in the article as well is that violation of the conservation of mass continuity within the elements is not checked. The amount of design variables in this approach is the amount of MM nodes times the amount of plies, where the amount of MM nodes depends on the complexity of the geometry and the load case.

2.1.3 Conclusion and answer to the question

Due to the obfuscated ply angles the LPA does not lend itself well for the problem at hand. A 2 dimensional solution that aims to quantify the effect of gaps and overlaps on the stiffness for the MMOA is in development. The approach also allows for the optimization to be strength based; however a method to move the approach in a 3 dimensional space must be found.

2.2 What is the effect of gaps and overlaps on the stiffness of a fibre steered laminate?

The gaps and overlaps created during steering need to be related to a change in stiffness. The effect of gaps and overlaps is assessed through the literature in which experiments have been done and recorded.

2.2.1 The effects of gaps and overlaps on the stiffness.

During the creation of an AFP steered laminate an initial tow is laid out. The next tow is laid offset from the previous tow. The tow-overlapping method results in overlaps which locally increase the thickness of the laminate. The tow-dropping method creates resin-rich regions. Depending on the strategy employed during the tow placement process, gaps and overlaps are created. To better understand the consequences of these defects, various studies have been conducted in regards to the strength.

Lopes [17] reports an increase in stiffness due to overlaps, while gaps create a reduction in stiffness. This makes sense as the thickness increases the stiffness increases. Gaps are areas where less fibers are available and this a reduction of stiffness is observed, Lopes adds a weight penalty to the calculation of the stiffness of the laminate. The results are shown in table 2.2, the layups are shown in table 2.1. The angles in this table are used to generate fibre paths as shown in Figure 2.2.

Arian Nik [18] created a variable stiffness laminate and discussed the effect of full overlaps and full gaps on the in-plane stiffness and buckling load.

Table 2.1: The stacking sequence of the laminates as discussed in 2.2

Design	Layup
(A)	$[\pm < 26/45/26 >]_{4S}$
(B)	$[\pm < 17/39/17 >]_{4S}$

As a result, gap regions have lower stiffness as compared to the unaltered composite material areas. Overlaps tend to generate stiffener-like features, which will carry higher load in comparison to to the areas with regular composite material. [7] [18]

Important of note is that the effect of gaps and overlaps on laminates in general is not limited to stiffness, as the stiffness changes so does the stress field on the plate. Aside from that the gaps and overlaps also affect the strength of the plate. To take this in account additional modification are required to the failure criteria applied during optimization for strength.

2.2.2 Deductions, assessment of the literature, and answer

From documented experiments in the literature the following can be concluded. A overlap increases stiffness, while a gap or resin-rich area reduces stiffness. After taking into account the weight penalty, there is no significant change in the penalized stiffness.

Table 2.2: In-plane stiffness and buckling load of designs (A) and (B) normalized with respect to the baseline considering the weight penalty. [3]

Laminate	Normalized stiffness	Normalized stiffness with weight penalty	Normalized buckling load	Normalized buckling load with weight penalty
Design (A) Ignoring defects	0.6	0.6	1.56	1.56
Design (A) Full overlap (8.93%)	0.66	0.61	2.05	1.88
Design (B) Ignoring defects	0.99	0.99	1.33	1.33
Design (B) Full overlap (10.40%)	1.10	1.00	1.84	1.67

2.3 Can a continuous correction function be found that corrects the stiffness during optimization in 3 dimensional space?

Multiple approaches are available to locate gaps and overlaps in a fibre steered ply. However none of those approaches have been implemented in a 3 dimensional space. The first approach is proposed by A. Blom.

2.3.1 Point based evaluation

To find gaps, Blom et al. [2] proposes a method to find tow-drop areas. Blom et al. finds whether a point is within a tow with the width of the tow. This method is computationally heavy as it finds which tow covers any given point, then the outermost point of the tow in question is checked with its neighbouring tow for overlap. The 0% coverage rule dictates that a tow drop should be formed, this means that this area has a low fibre density. The method in question allows for tow-drop areas to be found, however the method used is not suitable for the problem at hand. Blom et al. [2] also only find tow-drop areas, the methodology can be adjusted by checking if a point falls within a tow to find a gap. Knowing the course width and the centreline of the tow. This would allow the method to check for gaps and overlaps, however it would not solve the problem of requiring a relatively large amount of computing power. This makes it unsuitable for usage during the optimization.

2.3.2 Approaches using continuous functions

Fayazbakhsh [3] used a similar principle as described in section 3.3 of his dissertation to find the gaps in a 0% coverage strategy. Instead of using discrete points to find where gaps are in the ply, continuous functions were used to find the boundaries of each course. Using MATLAB, a subroutine was developed to calculate the intersection points of the course boundaries. When one edge is at the course boundary, the tow is cut perpendicular to the centreline.

The result is a gap in the ply. This provides a faster and more accurate way of finding the gaps. The same approach can be used to find the overlaps for a 100% coverage strategy. The boundary is deducted from the centreline, the equation for the centreline is shown in equation 2.3. In this equation T_0 is the angle as shown in Figure 2.2, ρ is the manufacturing radius, and x denotes the x-coordinate. The result is the y-coordinate of the centreline.

$$y_{centreline} = \sqrt{\rho^2 - (x - \rho cos(T_0))^2} - \rho sin(T_0) \tag{2.3}$$

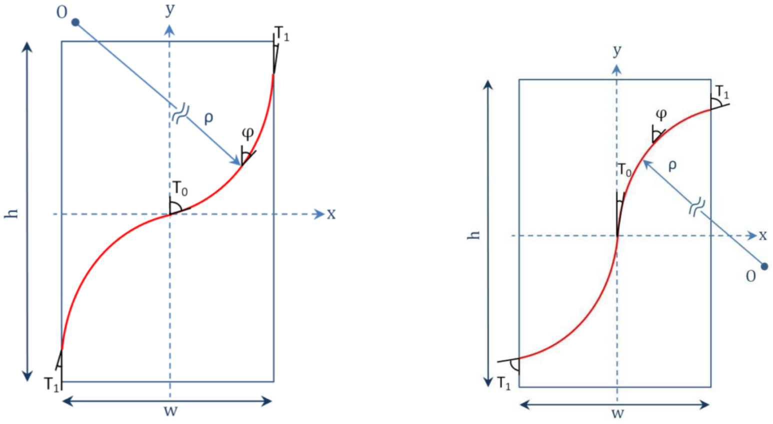

(a) **(b)**

Figure 2.2: Course centerline of a lamina $T_1 < T_0$ and $T_0 < T_1$ respectively Fayazbakhsh [2]

Using the assumption that the vertical distance between the bottom and top boundaries is constant, the gaps and overlaps can be found. The result of this approach can be seen in figure 2.3, the intersection points are shown in figure 2.3a. In figure 2.3b the gaps are shaded if the 0% coverage rule is applied, in figure 2.3c the overlaps are shaded if the 100% coverage rule is applied.

Lucas et al. [4] created an approach that uses the change in the fibre orientation angle. The research is a continuation of [9]. Following the recommendations of [1], in [4] a stiffness correction was introduced based on the change in fibre angle normal to the curve, as shown in Figure 2.4 and implemented in the post-processor. The relationship used for this correction is shown in equation 2.4. Where the change in density is related to a change in the fibre angle orientation.

$$\frac{\partial \rho}{\partial \mathbf{s}} = f\left(\frac{\partial \phi}{\partial \mathbf{n}}\right) \tag{2.4}$$

In which ϕ is the fibre angle orientation, and ρ is the density, which is a function of the changes in the fibre orientation angle normal to the curve. The orientation of the **n** and **s** are shown in figure 2.4. **s** is the direction tangent to the curve while **n** is normal to the curve.

The relation between the change in the fibre orientation angle normal to the curve and the density is simply taken to be a linear relation in the shape of equation 2.5 with k_c as a

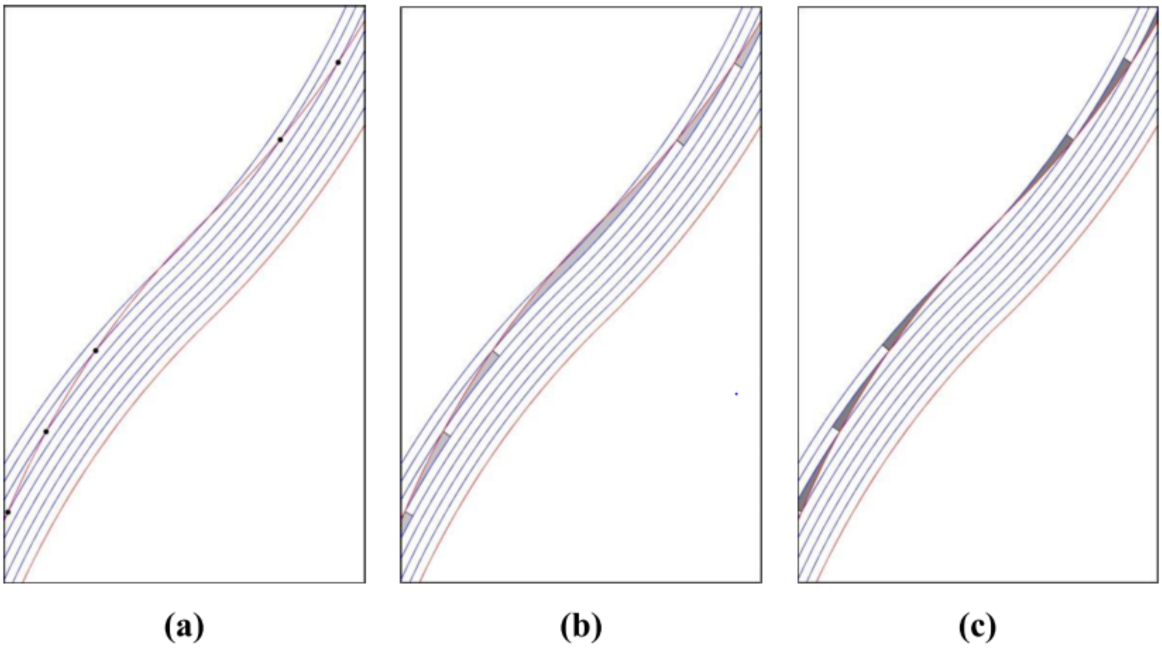

Figure 2.3: Gaps and overlaps as found by Fayazbakhsh [3]

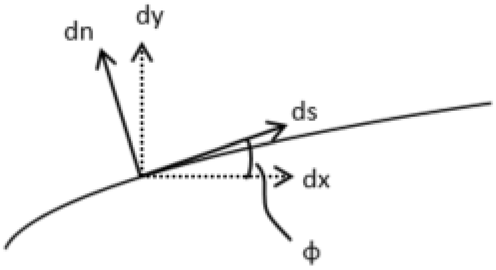

Figure 2.4: Tow path with 's' and 'n' directions [4]

constant. The author in [4] notes that: "The relationship should take more of a logarithmic functional shape".

$$\frac{\partial \rho}{\partial \mathbf{s}} = -k_c \frac{\partial \phi}{\partial \mathbf{n}} \tag{2.5}$$

This relation allows the manufacturing engineer to take into account the gaps and overlaps introduced by the fibre paths during optimization. Building on the stiffness correction factor of [4], van Tooren et al. [6] then implemented the stiffness correction factor in the optimization process.

2.3.3 Deductions, assessment of the literature, and answer

These methodologies for finding gaps and overlaps are 2D approaches to the problem at hand. The problem to be solved is in 3 dimensions. A continuous correction function can be found for 2D in current literature, both the methods proposed in [3] and [4] use continuous functions to find locations where the stiffness should be altered to account for manufacturing induced defects.

The methodology proposed by [4] was implemented to be used during the optimization process in [6]. The methodology has little overhead with respect to the other method proposed, additionally when a solution is found for moving the MMOA to 3D then this solution can be altered easily to work for the methodology proposed in [4].

Chapter 3

Methodology of the 3D multiple mesh approach

To optimize the fibre steered plies in the laminate of a curved plate, the approach of van Tooren [9] based on the first research question in section 2.1 was chosen. This optimization method is coined the multiple mesh optimization approach (MMOA) and optimization is done to maximize the buckling load or failure load given a number of plies in which the fibre angles can be varied. With this optimization method a program is created that allows the user to enter different geometries and load cases, and optimize the fibre steered laminate for the geometry with a supplied loadcase. The workflow shown in Figure 3.1 is outlining the steps that need to be taken to find a laminate with a maximized failure or buckling load.

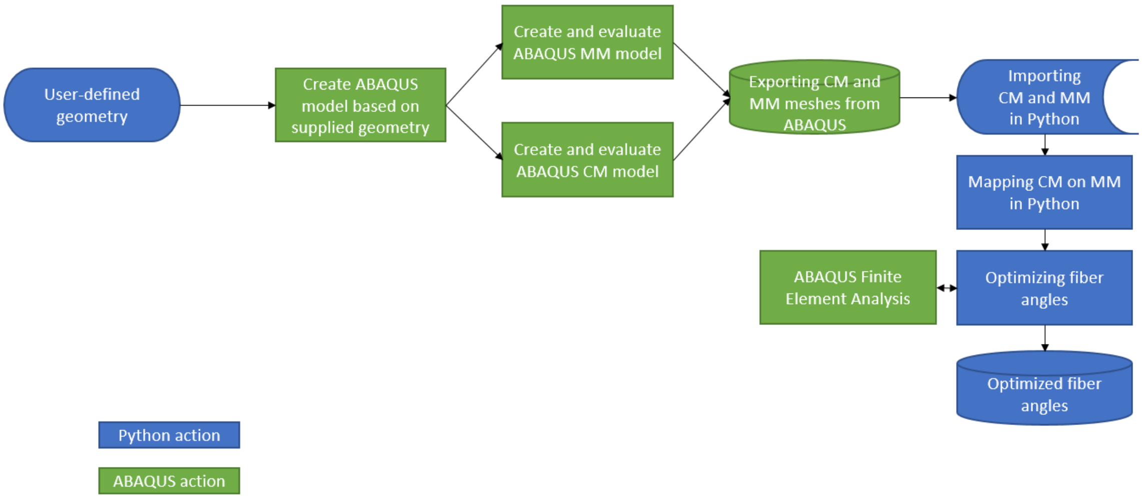

Figure 3.1: A high level overview of the order of the actions required to find a laminate optimized for a cost function

First the user-defined geometry is meshed in ABAQUS® to generate the calculation mesh (CM) and the manufacturing mesh (MM). In the nodes of the MM the design variables are defined as the fibre angles as shown in Figure 2.1. This coarser mesh is then used to find the fibre angles in the CM, and the CM is used to evaluate the stress problem. The two meshes are exported using .txt-file (ASCII code) format and saved in the working directory. These are then loaded in the TopSteer Python environment. The mapping procedure is initiated, the CM is mapped on the MM. The result of this procedure is a connection between the CM and MM, so that the fibre angles can be found in the CM for the ABAQUS® evaluation. This process is explained in sections 3.1 through 3.3.

The results are fed into the optimization procedure, which uses the connection between the two meshes and Lagrangian interpolation to distribute the fibre angle onto the CM. The optimization procedure uses the boundary condition, loads and fibre angles on the CM and generates an input file for ABAQUS®. This input file is evaluated and after applying a failure criteria, the maximum value is returned to the optimizer. This process describes one evaluation, and these steps are described in more detail in sections 3.4 throught 3.6.

3.1 Identifying CM centroids within MM elements

To identify which CM element and lies within which MM element, the distance between the centroids of the CM elements and MM elements is used. All the CM elements lie within a MM element and none are located outside of the MM, because the meshes are generated on the same surface in ABAQUS® as shown in Figure 3.2. The green dots represent the centroids of the MM elements of which 4 are displayed, the orange dots are the centroids of the CM elements. A CM element lies within a MM if the distance between the centroid of the CM element and the centroid of its MM element is smaller than the distance between the centroid of the CM element and the centroid of the other MM elements. For this to work, the location of the centroid of the elements is required as well as a method to find the distance between two points.

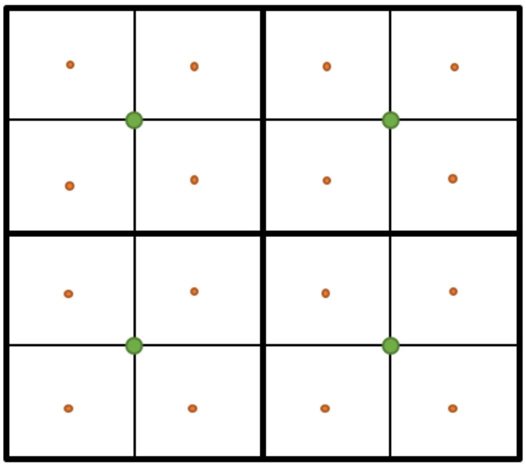

Figure 3.2: A simplified visual representation of the MM with the CM and their centroids

First the centroid of a quadrilateral element of any shape is found as explained in section 3.1.1 then relating the CM to the MM is discussed in section 3.1.2.

3.1.1 Finding centroids of quadrilateral element in 3D space

The centroids of the mesh elements are not available in ABAQUS®, however using the node locations of a quadrilateral element the centroid can be found. The quadrilateral element is split in 2 triangular elements as shown in Figure 3.3. The coordinates of the centroid G of the triangular element ABC can be found by using Eq. (3.1).

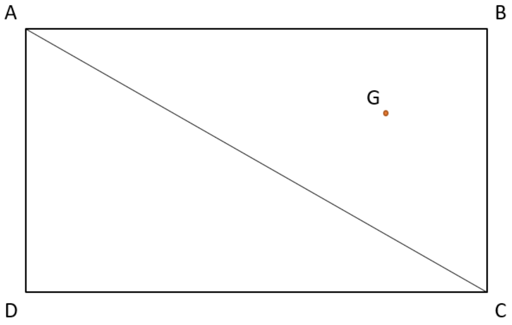

Figure 3.3: A quadrilateral element in triangular elements.

$$G = \frac{A + B + C}{3} \tag{3.1}$$

In this equation $A = [A_x, A_y, A_z]$ $B = [B_x, B_y, B_z]$, and $C = [C_x, C_y, C_z]$ are the locations of the vertices of the triangular element. $G = [G_x, G_y, G_z]$ is the location of the centroid of the triangular element. By taking the weighted average of the centroid with their area as described in Eq. (3.2) the centroid of the quadrilateral element $H = [H_x, H_y, H_z]$ can be found.

$$H = \frac{\sum_{i=1}^{n} G_i A_i}{\sum_{i=1}^{n} A_i} \tag{3.2}$$

In this equation A_i denotes the area of the triangular element, n will be 2 since the quadrilateral element is is split into 2 triangular elements. To find the area, two vectors ($\boldsymbol{\beta}$ and $\boldsymbol{\gamma}$) that share the same initial point (A) are created. These vectors are defined as $\boldsymbol{\beta} = B - A$ and $\boldsymbol{\gamma} = C - A$ Then the area (S) of the parallelogram defined by $\boldsymbol{\beta}$ and $\boldsymbol{\gamma}$ is defined by Eq. (3.3).

$$S = |\boldsymbol{\beta} \otimes \boldsymbol{\gamma}| \tag{3.3}$$

Given that the area of the triangular element will be half the area of the parallelogram and Eq. (3.3) describes the area of a parallelogram. The area of the triangular element is found using 3.4

$$S = \frac{1}{2}|\boldsymbol{\beta} \otimes \boldsymbol{\gamma}| \tag{3.4}$$

With the area of each triangular element known, the centroid of a quadrilateral element can be calculated using Eq. (3.2).

Verification of the methodology used to find the centroids To ensure the validity of the approach differently shaped quadrilateral elements have been evaluated. The 2D cases evaluated are described in Appendix B. The elements chosen have centroid which can be found through alternate means. The first element is a rectangular element set at a 45^o incline, the nodes of the element are as given in Table 3.1 and the element and its centroid is graphically represented in Figure 3.4.

Table 3.1: Coordinates for a square surface at an 45^o degree angle

	x	y	z
node 1	0	0	0
node 2	1	0	0
node 3	1	1	1
node 4	0	1	1

As this the same element as previously evaluated but under a 45^o degree angle, the centroid is expected to be at $[0.5, 0.5, 0.5]$. The centroid finding approach locates the centroid at $[0.5, 0.5, 0.5]$. Agreeing with the centroid location.

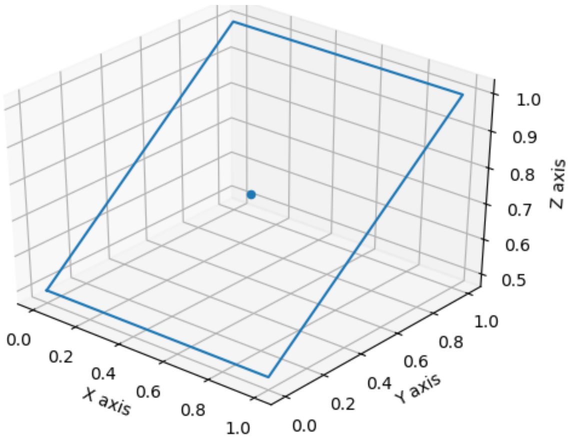

Figure 3.4: Square surface at an 45^o degree angle with its centroid.

A 3D wedge is evaluated to simulate heavily deformed elements, the nodes of the element are given in Table B.2.

Table 3.2: Coordinates for a wedge surface at an 45^o degree angle

	x	y	z
node 1	0	0	0
node 2	0	1	0
node 3	1	0.5	1
node 4	1	0.5	1

The methodology finds the centroid at $[0.333, 0.5, 0.333]$. With the formula of the centroid of a triangle, it can be concluded that this is correct.

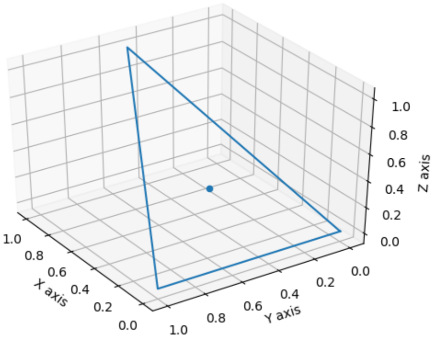

Figure 3.5: A wedge shaped surface at 45^o degree angle with its centroid

3.1.2 Distance between centroids

The MM element in which a CM element is located can now be found by finding minimum distance between the centroid of the CM element with respect to each MM element. The distance between two centroids, c_1 and c_2 in a 3 dimensional space is calculated using Eq. (3.5).

$$d = \sqrt{(x_1 - x_2)^2 + (y_1 - y_2)^2 + (z_1 - z_2)^2} \tag{3.5}$$

Given the location of the CM centroid in its respective MM element the interpolation procedure can be started if this was 2D case. However in 3D few interpolation procedures become more complex and would need to be done for every evaluation of the problem during the optimization procedure. Instead the choice is made to move the MM element and the CM centroids contained in it to a 2D iso-parametric space. This trivializes the interpolation procedure.

3.2 Rotating the MM element and it CM centroids

To move the problem to a 2 dimensional space the MM elements are rotated to be in one plane. The unit vector normal to the MM element is found and then the unit vector normal to the xy-plane a rotation matrix is found. The unit normal vector of a MM element is assumed to be the average of the unit normal vectors in all the nodes of the element. The normal vector of the MM element can be found by Eq. (3.6).

$$\boldsymbol{n} = \frac{\boldsymbol{\beta} \otimes \boldsymbol{\gamma}}{||\boldsymbol{\beta} \otimes \boldsymbol{\gamma}||} \tag{3.6}$$

In this equation AB is $\mathbf{B} - \mathbf{A}$ and AC is $\mathbf{C} - \mathbf{A}$.

To find the rotation matrix, Rodrigues' rotation formula is used, the formula is shown in (3.7).

$$\boldsymbol{R} = \boldsymbol{I} + \sin(\theta)\boldsymbol{V_x} + (1 - \cos(\theta))\boldsymbol{V_x}^2 \tag{3.7}$$

In this formula $\boldsymbol{R}$ represent the rotation matrix; θ is the angle by which a vector $\boldsymbol{a}$ is rotated around a unit vector $\hat{\boldsymbol{v}}$. $\boldsymbol{I}$ is representing the identity matrix; $\boldsymbol{V_x}$ is the skew-symmetric cross-product matrix of $\hat{\boldsymbol{v}}$.

$$\boldsymbol{V_x} = \begin{bmatrix} 0 & -\hat{\boldsymbol{v}}_3 & \hat{\boldsymbol{v}}_2 \\ \hat{\boldsymbol{v}}_3 & 0 & -\hat{\boldsymbol{v}}_1 \\ -\hat{\boldsymbol{v}}_2 & \hat{\boldsymbol{v}}_1 & 0 \end{bmatrix} \tag{3.8}$$

The normal unit vector ($\boldsymbol{a}$) of the MM element is found using Eq. (3.6) and the unit vector of the xy-plane $[0, 0, 1]$ ($\boldsymbol{b}$). To find the rotation matrix that rotates $\boldsymbol{a}$ onto $\boldsymbol{b}$ the unit vector $\hat{\boldsymbol{v}}$ needs to be found as a function of the vectors $\boldsymbol{a}$ and $\boldsymbol{b}$. This vector ($\hat{\boldsymbol{v}}$) has to be orthogonal to be $\boldsymbol{a}$ and $\boldsymbol{b}$ and can be found using Eq. (3.9).

$$\boldsymbol{v} = \frac{\boldsymbol{a} \otimes \boldsymbol{b}}{||\boldsymbol{a} \otimes \boldsymbol{b}||} \tag{3.9}$$

With $\sin(\theta) = ||\boldsymbol{a} \otimes \boldsymbol{b}||$ and substituting this into Eq. (3.7) results in Eq. (3.10)

$$\boldsymbol{R} = \boldsymbol{I} + \boldsymbol{V_x} + \frac{(1 - \cos(\theta))}{\sin(\theta)} \boldsymbol{V_x}^2 \tag{3.10}$$

The rotation matrix is applied to rotate MM elements and the associated CM centroids to the xy-plane as shown in Eq. (3.11).

$$\boldsymbol{u_{rot}} = \boldsymbol{Ru} \tag{3.11}$$

A different way of finding the same rotation matrix is through the usage of a basis change, this process yields the same rotation matrix as a result and is explained in A.

3.2.1 Verification of the rotation methodology

To ensure that the rotation matrix that is created using the methodology described in section 3.2 a simple test is conducted. An element with the nodes as described in Table 3.3 is created and rotated into the xy-plane.

Table 3.3: Coordinates inclined example MM element

	x	y	z
node 1	1	0	0
node 2	1	1	0
node 3	0	0	1
node 4	0	1	1

To do so first a unit vector normal to the xy-plane is defined. The original element is shown as the blue square in Figure 3.6, the unit vector normal to the x-plane is the red line. The yellow line shows the unit normal vector to the original MM element which is calculated with Eq. (3.6). Now the rotation matrix can be calculated with equation Eq. (3.10), after which the element can be rotated using Eq. (3.11). The rotated element is displayed in Figure 3.6 as the purple square.

This allows for the MM elements and their CM centroids to moved onto the xy-plane. However the shape of the element is not the same for each element, and not necessarily defined to be square or rectangular. To aid the interpolation procedure this is desirable. In the next section this problem is resolved by moving it into iso-parametric space.

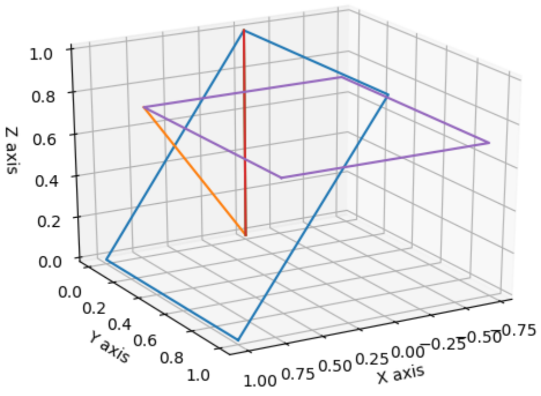

Figure 3.6: Figure showing the vectors and elements involving rotation of the MM element

3.3 Moving into iso-parametric space.

To ensure that the interpolation works on oddly shaped elements, the rotated MM elements are moved into iso-parametric space. The procedure of moving from the global coordinate system into the natural coordinate system is well establish and was introduced by Taig [19] in 1961 as shown in Eq. (3.12).

$$x(\xi,\eta) = \sum_{i=1}^{4} N_i(\xi,\eta)x_i, \qquad y(\xi,\eta) = \sum_{i=1}^{4} N_i(\xi,\eta)y_i \tag{3.12}$$

Here ξ and η are the natural coordinates, and x and y are the global coordinates. The node numbering system as shown in Figure 3.7 is employed to find the Lagrangian shape functions as presented Eq. (3.13).

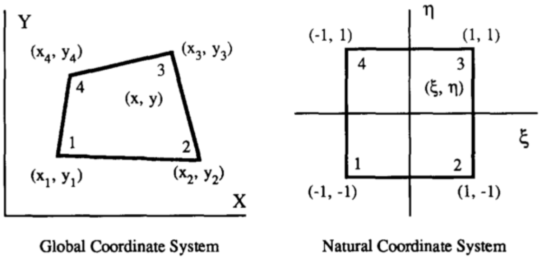

Figure 3.7: Figure describing the node numbering order in the global and natural coordinate system [5]

$$\begin{aligned} N_1(\xi,\eta) &= \frac{1}{4}(1-\xi)(1-\eta), & N_2(\xi,\eta) &= \frac{1}{4}(1+\xi)(1-\eta) \\ N_3(\xi,\eta) &= \frac{1}{4}(1+\xi)(1+\eta), & N_4(\xi,\eta) &= \frac{1}{4}(1-\xi)(1+\eta) \end{aligned} \tag{3.13}$$

Substituting Eq. (3.13) into Eq. (3.12) then the following relation is found between x, y, ξ, and η.

$$\begin{aligned} x &= \frac{x_1}{4}(1-\xi)(1-\eta) + \frac{x_2}{4}(1+\xi)(1-\eta) + \frac{x_3}{4}(1+\xi)(1+\eta) + \frac{x_4}{4}(1-\xi)(1+\eta) \\ y &= \frac{y_1}{4}(1-\xi)(1-\eta) + \frac{y_2}{4}(1+\xi)(1-\eta) + \frac{y_3}{4}(1+\xi)(1+\eta) + \frac{y_4}{4}(1-\xi)(1+\eta) \end{aligned} \tag{3.14}$$

The inverse transformation is generally not considered in the finite element literature. Using geometric considerations a complete set of general solutions can be derived as shown by Hua [5]. By inversing Eq. (3.13) the relationship between the natural and global coordinate systems for quadrilateral isoparametric elements can be written as Eq. (3.14). This bilinear system of equations can not be solved generally [5]. To write the system of equations compactly a, b, c, and d have been defined as shown in Eq. (3.16) and Eq. (3.15). Then terms containing ξ, η, and $\xi\eta$ can be seperated. The definition of these variables depends on the node numbering scheme in the natural coordinates system, which is shown in Figure 3.7.

$$\begin{aligned} d_1 &= 4x - (x_1 + x_2 + x_3 + x_4) \\ d_2 &= 4y - (y_1 + y_2 + y_3 + y_4) \end{aligned} \tag{3.15}$$

$$\begin{bmatrix} a_1 & a_2 \\ b_1 & b_2 \\ c_1 & c_2 \end{bmatrix} = \begin{bmatrix} 1 & -1 & 1 & -1 \\ -1 & 1 & 1 & -1 \\ -1 & -1 & 1 & 1 \end{bmatrix} \begin{bmatrix} x_1 & y_1 \\ x_2 & y_2 \\ x_3 & y_3 \\ x_4 & y_4 \end{bmatrix} \tag{3.16}$$

Using Eq. (3.16) and Eq. (3.15), Eq. (3.14) can be rewritten to Eq. (3.17).

$$\begin{bmatrix} b_1 & c_1 \\ b_2 & c_2 \end{bmatrix} \begin{Bmatrix} \xi \\ \eta \end{Bmatrix} = \begin{Bmatrix} d_1 - a_1\xi\eta \\ d_2 - a_2\xi\eta \end{Bmatrix} \tag{3.17}$$

The system as defined by Eq. (3.17) can not be solved unless additional conditions on the system are imposed. To make the process easier the determinant of a 2 by 2 matrix is defined as in Eq. (3.18).

$$r_s = \begin{vmatrix} r_1 & s_1 \\ r_2 & s_2 \end{vmatrix} = r_1 s_2 - r_2 s_1 \tag{3.18}$$

In this equation, r and s can be replaced with the a, b, c and d from Eq. (3.16). In the following paragraphs, different conditions will be discussed.

Condition: $a_1 = 0$**,** $a_2 = 0$ In this case the Eq. (3.17) becomes a linear system and reduces to Eq. (3.19)

$$\xi = \frac{d_c}{a_1 d_2 + b_c} \qquad \eta = \frac{b_d}{a_2 d_1 + b_c} \tag{3.19}$$

Condition: $a_1 = 0$, $a_2 \neq 0$ Now Eq. (3.17) is not solveable unless conditions are imposed on c_1. If $c_1 = 0$ then the solution is as given by Eq. (3.20).

$$\xi = \frac{d_1}{c_1} \qquad \eta = \frac{b_d}{a_2 d_1 + b_1 c_2} \tag{3.20}$$

If $c_1 \neq 0$ then the solution is as given by Eq. (3.21). Note that the solution for $\xi \in [-1.0, 1.0]$.

$$0 = a_2 b_1 \xi^2 + (c_b - a_2 d_1)\xi + d_c \qquad \eta = \frac{d_1 - b_1 \xi}{c_1} \tag{3.21}$$

Condition: $a_1 \neq 0$, $a_2 \neq 0$ If $a_b \neq 0$ and $a_c \neq 0$ Eq. (3.22) will provide a solution. Note that the solution for ξ should be ϵ $[-1.0, 1.0]$

$$a_b \xi^2 + (c_b + d_a)\xi + d_c = 0 \qquad \eta = \frac{a_d + b_a \xi}{a_c} \tag{3.22}$$

If instead $a_b \neq 0$ and $a_c = 0$ then Eq. (3.23) will allows for a solution to the inverse transformation.

$$\xi = \frac{a_d}{a_b} \qquad \eta = \frac{a_1 d_b}{c_1 a_b + a_1 a_d} \tag{3.23}$$

If $a_b = 0$ then a_c must be 0 resulting in Eq. (3.24).

$$\xi = \frac{a_1 d_c}{b_1 a_c + a_1 a_d} \qquad \eta = \frac{a_d}{a_c} \tag{3.24}$$

Condition $a_2 = 0$ **and** $c_2 \neq 0$ In this case the expression for the solutions depends on b_2, if $b_2 = 0$ then:

$$\xi = \frac{d_c}{a_1 d_2 + b_1 c_2} \qquad \eta = \frac{d_2}{c_2} \tag{3.25}$$

If instead $b_2 \neq 0$ then the following formulas can be used to find a solution.

$$a_1 b_1 \xi^2 + (c_b - a_1 d_2)\xi +_c = 0 \qquad \eta = \frac{d_2 - b_2 \xi}{c_2} \tag{3.26}$$

To verify that the transformation to the natural coordinate system works as intended the 8 different conditions are evaluated. The point for which the problem is evaluated is the average of the nodes of the quadrilateral element. In the natural coordinate system this should result in point at $[0, 0]$. To keep the main body short this section is available for review in C.

3.4 Interpolation

Now that the MM element and the CM centroids associated with the MM element are in the natural coordinate system, interpolation the fibre angles upon the centroids from the nodes of the MM is elementary. For the purpose of interpolation a simple Lagrangian interpolation is used. The fibre angle definition and node numbering scheme are shown in Figure 3.8.

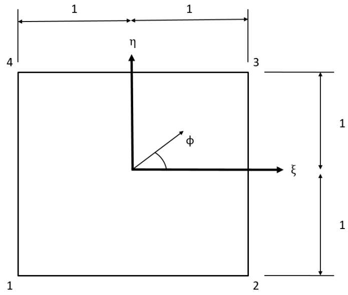

Figure 3.8: The MM element after rotation and inverse parametric mapping with the fibre angle

The fibre angle as a function of ξ and η in the MM element d is:

$$\phi^{(d)} = \sum_{i=1}^{n} N_i^d(\xi,\eta)\phi_i^d \tag{3.27}$$

In Eq. (3.27) the N_i^e terms are the general shape functions for Lagrangian interpolation as described in the following equations. Assuming the node numbering as shown in Figure 3.8 is adhered to. i is used to denote the node number.

$$N_1^{(d)}(\xi,\eta) = \frac{x - x_2}{x_1 - x_2}\frac{y - y_4}{y_1 - y_4} \tag{3.28}$$

$$N_2^{(d)}(\xi,\eta) = \frac{x - x_1}{x_2 - x_1}\frac{y - y_3}{y_2 - y_3} \tag{3.29}$$

$$N_3^{(d)}(\xi,\eta) = \frac{x - x_4}{x_3 - x_4}\frac{y - y_2}{y_3 - y_2} \tag{3.30}$$

$$N_4^{(d)}(\xi,\eta) = \frac{x - x_3}{x_4 - x_3}\frac{y - y_1}{y_4 - y_1} \tag{3.31}$$

These equations are valid for a general 4 node rectangular element. Since the element is an isoparametric element, the element is square and the values for $x_1 \ldots x_4$ and $y_1 \ldots y_4$ are known. This reduces the equation for the shape functions to Eq. (3.32) through Eq. (3.35).

$$N_1^{(d)}(\xi,\eta) = \frac{(1-\xi)(1-\eta)}{4} \tag{3.32}$$

$$N_2^{(d)}(\xi,\eta) = \frac{(1+\xi)(1-\eta)}{4} \tag{3.33}$$

$$N_3^{(d)}(\xi,\eta) = \frac{(1+\xi)(1+\eta)}{4} \tag{3.34}$$

$$N_4^{(d)}(\xi,\eta) = \frac{(1-\xi)(1+\eta)}{4} \tag{3.35}$$

These shape equations and Eq. (3.27) interpolate the fibre angles in the CM elements. The ABAQUS® model is evaluated with the fibre angles in the CM.

3.5 Failure criterion

In the optimization procedure a Pythonfunction that takes the stress of an element and calculates the failure index build in a modular fashion. This allows the user to change the failure criterion used effortlessly. The failure criterion used in the optimization is the Tsai-Wu failure criterion. The formula for this criterion is given in 3.36.

$$FI = \left(\frac{\sigma_{11}}{S_{11}}\right)^2 + \left(\frac{\sigma_{22}}{S_{22}}\right)^2 - \left(\frac{\sigma_{11}\sigma_{22}}{S_{11}^2}\right)^2 + \left(\frac{\sigma_{12}}{S_{12}}\right)^2 \tag{3.36}$$

The applied load is a unit load, the failure index is used as an indication of how well the current fibre steered layup performs. The problem is optimized by minimizing the maximum failure index present in the model. The stress based failure criteria are based on the classical laminated plate theory (CLPT) thus neglecting inter-laminar shear stresses and stresses through the thickness, instead failure criteria that incorporate these stresses can be evaluated. Failure mode based failure criteria are a way of improving how well the failure criteria mimics reality, some of these are the NASA developed LaRC05 and the Puck 3D failure criteria.

3.6 Optimization algorithm

For the optimization the Python package SciPy is used. Within SciPy the method sequential least squares programming is used to set up a minimization function. The function uses sequential quadratic programming. [20]

Chapter 4

Implementation of the 3D multiple mesh approach

In this chapter the implementation of the multiple mesh optimization approach (MMOA) is presented, the theory is discussed in 3. First the pre-processing is discussed in 4.1, and the optimization procedure is discussed in 4.2.

4.1 Pre-processing

During pre-processing two main activities are performed. Initially the model that is evaluated is created and the manufacturing mesh (MM) and calculation mesh (CM) are generated, this process is discussed in the next section. In the following section the work flow for the mapping process is shown. The results of the pre-processing are discussed to finalize this section.

4.1.1 Model and mesh generation

First in ABAQUS® a geometry is imported or created in the ABAQUS® graphical user interface (GUI). The next step is to provide material properties and define a composite layup in the *property* module in ABAQUS®. The composite layup does not need to contain any values, and any properties entered in the composite layup definition will be discarded during optimization. The only thing that is kept is the layup orientation. So this should be specified in the ABAQUS® GUI correctly.

The next step is to specify the step in ABAQUS®. For a linear buckling analysis the procedure type is changed to a *Linear perturbation* and then a *buckle* step is chosen. For tensile or shear optimization a *Static, General* procedure is chosen.

In the *Load* module of the ABAQUS® GUI the loads and boundary conditions are defined. After this step the model must be copied within the ABAQUS® environment. On the geometry of the first model the MM is generated while the problem is evaluated on the surface of the second model which has a finer CM. Both the models are evaluated and the **.odb** files are made accessible for the mapping process.

4.1.2 Mapping process

The goal is to apply an interpolation process to move the fibre angles from the MM to the CM to do this the two meshes need to be linked. This is done using the mapping process shown in the work flow in Figure 4.1.

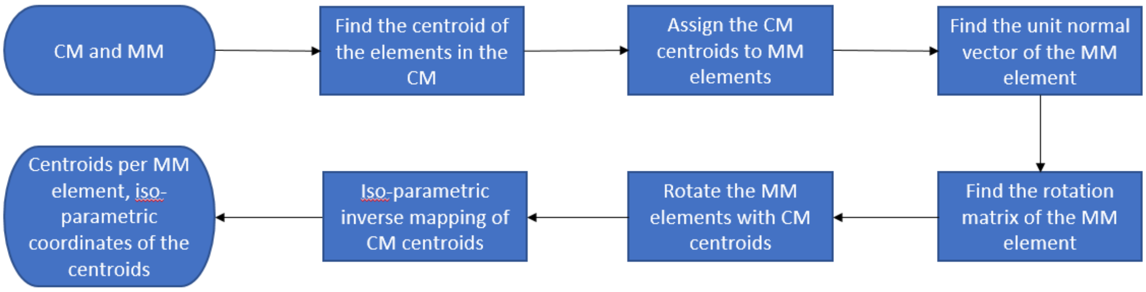

Figure 4.1: Work flow describing the mapping process

First the CM and MM are loaded from the **.odb** files as created by the previous process. These are used with the methodology described in section 3.1.1 to find the centroids of both of the meshes. The centroids are used with the methodology described in section 3.1.2. The distance between the centroid of each CM from each MM found, then the CM elements are assigned to the MM elements in which the lie. This results in a array containing the CM element numbers that are in the MM element.

The MM element normal unit vector is determined as described in section 3.2 with Eq. (3.6). The rotation matrix is found with Eq. (A.7) – (A.9). Equation (A.10) rotates all of the vertices of the MM elements and the centroids of the CM elements associated with the MM element as found earlier.

The process as described in section 3.3 finds the coordinates of the CM centroids in the natural coordinate system.

4.1.3 Results

The results are saved so that during each evaluation of the simulation this process does not have to be repeated. After the mapping procedure the location of the centroid CM in iso-parametric space is saved with the MM element in which the CM is located. During the optimization process the mapping procedure will not have to be repeated, instead only the interpolation procedure required for each evaluation.

4.2 Optimization

This section the optimization procedure and implementation is discussed, first the input required for the optimization to start is treated. The optimization work flow is elaborated upon in the next section. Finally the results are saved and made ready for the next step is outlined.

4.2.1 Input

For the optimization procedure the following data is required. First is the result of the mapping procedure as explained in section 4.1. Additionally the .inp file of the CM model is required as this file is adapted to generate the .inp file that is loaded into ABAQUS® during every evaluation. In the script the initial layup and which plies are allowed to be steered have to be defined.

4.2.2 Optimization loop

The work flow diagram of the optimization loop is shown in Figure 4.2. The first step, as shown in the bottom of the work flow diagram, is to find the fibre angles in the centroids of the CM elements. With the density function activated, the fibre angles in the MM nodes will also be determine the knockdown factor added to the material properties which represents a change in stiffness due to a gap or overlap. The density function alters the material properties for each element. This process will be further discussed in chapter 6. The new material properties are then set into the .inp file.

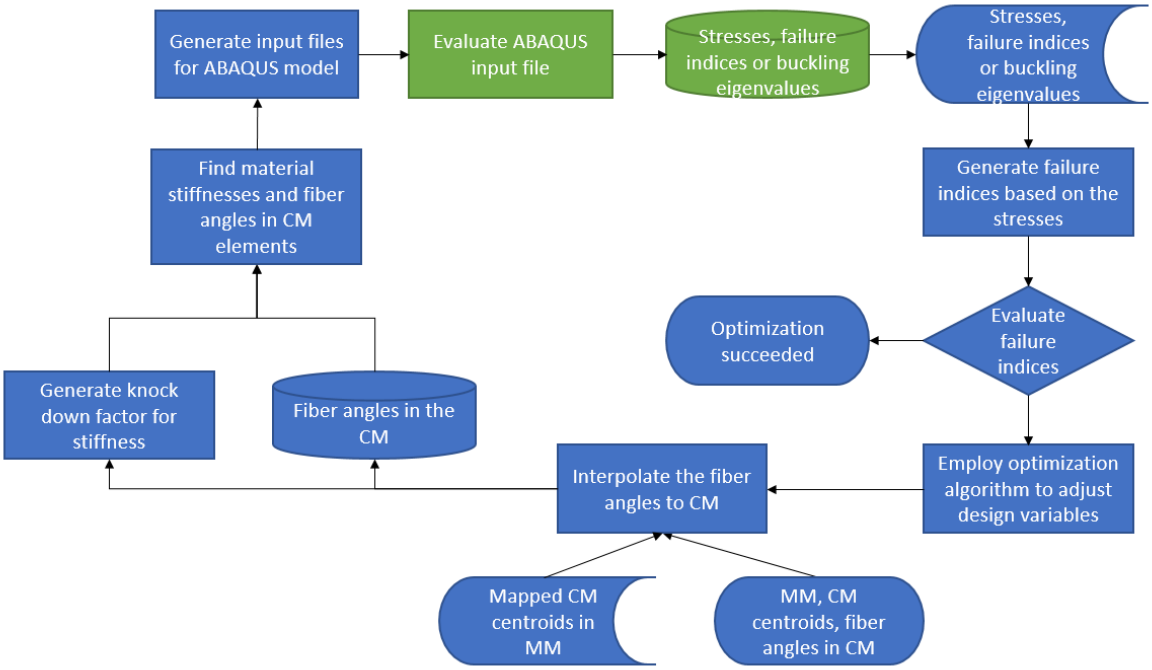

Figure 4.2: Work flow of the cost function of the optimization loop

ABAQUS® then evaluates the .inp file created by the Python script. These steps are executed in ABAQUS® as indicated by the green steps in Figure 4.2. ABAQUS® exports the stresses and failure indices or buckling eigenvalue to .txt files. The optimization algorithm then uses the evaluation together with the other evaluations in the current iteration to check for convergence, if the optimizer deems the problem to be converged it exits the optimization and saves fibre angles of the MM in a .txt file. Otherwise the fibre angles in the MM nodes are adjusted, and another iteration is started.

4.2.3 Results

The result of the optimization is a .txt file containing the fiber angles in the MM nodes, the location of the MM nodes and the element connectivity. This allows for the next step to be done without the need for other data to be read by the post-processor. The post-processor uses Lagrangian interpolation to find the tow paths that the automated fibre placement (AFP) machine will lay. A visual representation of these tow paths shows the results of the optimization.

Chapter 5

Verification of the 3D multiple mesh approach

To verify the implementation of the multiple mesh optimization approach (MMOA) two cases are taken from the literature, the first is a simple tensile case. The tensile case is discussed in section 5.1. The second case is by applying a compression load and optimizing for buckling through the buckling eigenvalue. This is discussed in section 5.2Results from the literature are used to verify the results acquired from the optimization

5.1 Tensile

5.1.1 Problem description

The tensile problem taken from the literature. The problem is described by Barazanchy [1]. The same boundary conditions are applied to the model in the ABAQUS® graphical user interface (GUI) as described in section 4.1.

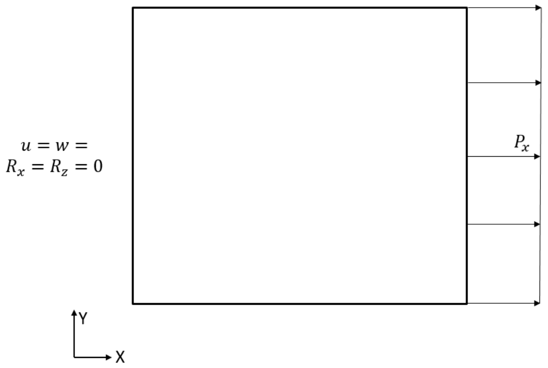

Figure 5.1: Boundary conditions for the tensile load maximization

The left side of the plate is constrained in the x-direction, z-direction, rotation around x-axis, and the rotation around y-axis as shown in Figure 5.1. The remainder of the edges remain free. A unit load is applied to the right surface. The manufacturing mesh (MM) used for this problem is shown in Figure 5.2 (a) and the calculation mesh (CM) is shown in Figure 5.2 (b).

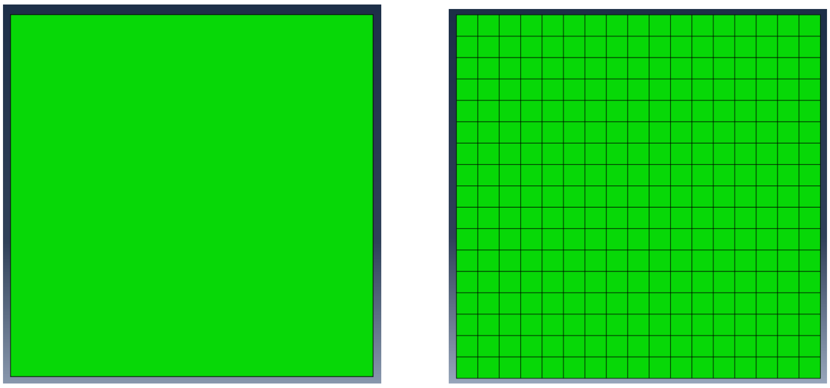

(a) The MM consisting of a single element

(b) The CM a 17 by 17 mesh.

Figure 5.2: The meshes for the tensile load maximization

5.1.2 Optimization results and discussion

The expectation is that the fibres align with the direction of the loading. Hence the fibres should move to the 0^o direction. To ensure that the algorithm works, multiple different starting points are used; the different attempts and their results are shown in Table 5.1. The first column shows the initial lay-up given to the optimization algorithm. The second column provides the average fibre angle in that ply that is returned by the optimization script. This is done because the values for the fibre angle are very close.

Table 5.1: Optimization results for the tensile test case using different starting variables

	Starting lay-up	Optimized lay-up
Case 1	[0]	[0.0]
Case 2	[45]	[3.36e-05]
Case 3	[90]	[179.98]
Case 4	[45 / 90]	[179.96 / 179.96]
Case 5	[45 / 90 / 135]	[0 / 0 / 0]

The results are clear, the optimizer attempts to put the plies in the 0^o direction as expected for any of the attempted starting layups.

5.2 Buckling

After the verification using a simple tensile problem. A buckling problem is proposed, optimized and compared against available literature.

5.2.1 Problem description

The next case is a plate loaded in compression. To reduce the amount of design variables for the optimizer the laminate is kept symmetric and balanced. The optimization aims to maximize the buckling load based on the buckling eigenvalue for the given layup. The following configuration is considered $[\theta_1, -\theta_1, -\theta_1, \theta_1]$. Here θ_1 denotes a array containing the fibre angles on the MM elements.

The model is given a unit load on the right side of the square. The boundary conditions are defined as in Figure 5.3 by Reddy [21].

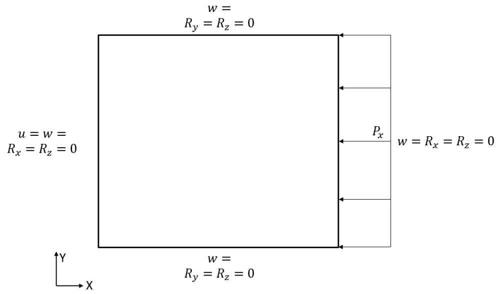

Figure 5.3: Boundary conditions for the buckling load maximization

The buckling boundary conditions are as follows. For the left side of the plate $u = w = 0$ the rotations around x and z are constrained. This enforces that the edges remain straight. For the right edge of the plate the boundary conditions are the same, however u is not constrained since there a compressive force is applied in the x-direction there. The top and bottom edge have their displacements in w constrained and the rotation around the y and z axis are constrained as well.

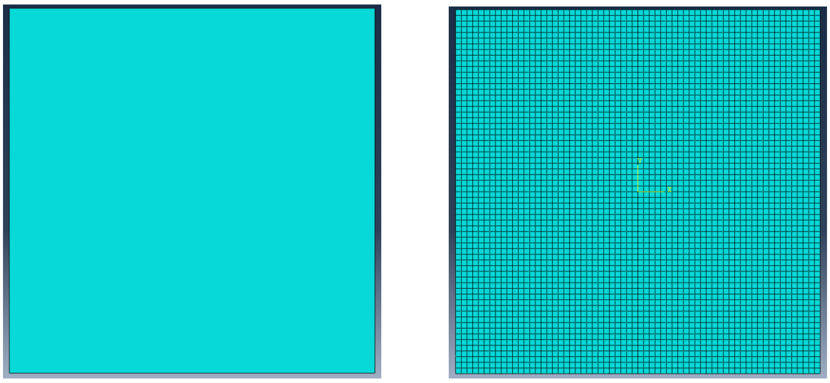

(a) The single element MM

(b) The CM for which the problem is evaluated

Figure 5.4: The meshes for the buckling load maximization

For the next part of the verification the MM is changed to a 2 by 2 mesh and a 3 by 3 mesh as shown in Figure 5.5.

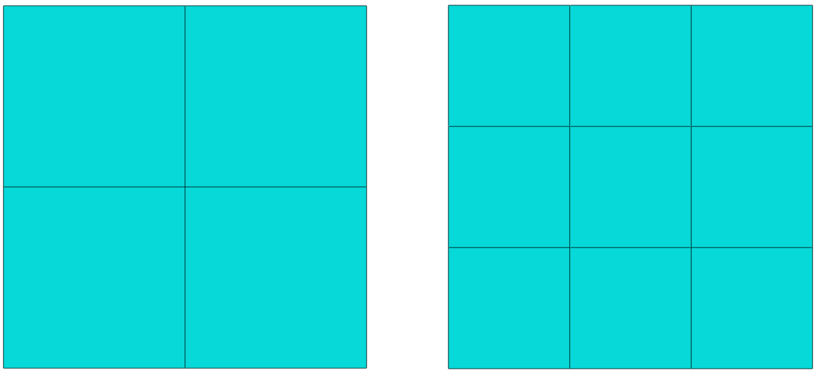

(a) The 2 by 2 MM **(b)** The 3 by 3 MM

Figure 5.5: Two alternative MM evaluated

5.2.2 Optimization results and discussion

For a single MM element the result is expected to be plies containing 45^o angles if the plate is square and the laminate is symmetric and balanced [22].

Table 5.2: Optimized layup for the buckling load case with a single MM element with different starting layups

	Starting layup	Optimized layup
Case 1	[0/0/0/0]	[45/-45/-45/45]
Case 2	[-37/37/37/-37]	[-44/44/44/-44]
Case 3	[-90/90/90/-90]	[-45/45/45/-45]
Case 4	[37/-37/37/-37]	[-46/46/46/-46]
Case 5	[90/-90/-90/90]	[-46/46/46/-46]

Table 5.2 presents the layup after optimizing for the buckling load. Confirming that the optimization procedure finds the solution that has the highest buckling load.

A MM containing multiple elements can start taking advantage of fibre steering. Figure 5.5 shows the additional MMs for which the buckling optimization was evaluated.

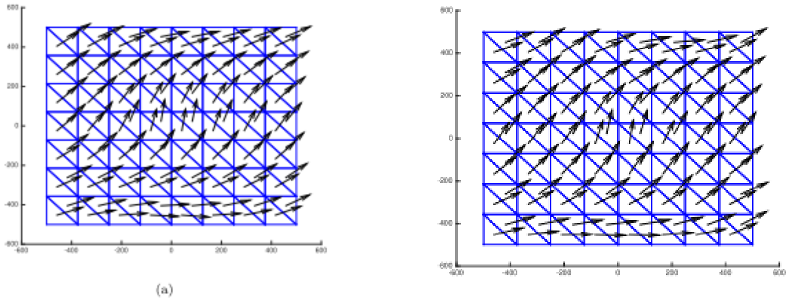

(a) with a 3 by 3 MM mesh

(b) with a 4 by 4 MM mesh

Figure 5.6: Results of maximizing for the buckling load [1]

This buckling load case has been evaluated by **insert names** [1] [23] [24]. According these articles the fibres in the ply move towards a S shape as shown in Figure 5.6. The seed points are on the diagonal of the plate running from top left to bottom right. Figure 5.7(a) shows the results of the 2 by 2 MM and Figure 5.7(b) for a 3 by 3 MM. As before the aim of the optimization is to maximize the buckling load. In these optimizations the laminate layup is set to be $[\theta, -\theta, -\theta, \theta]$. So that effectively only a single ply is designed and the resulting laminate is balanced and symmetric.

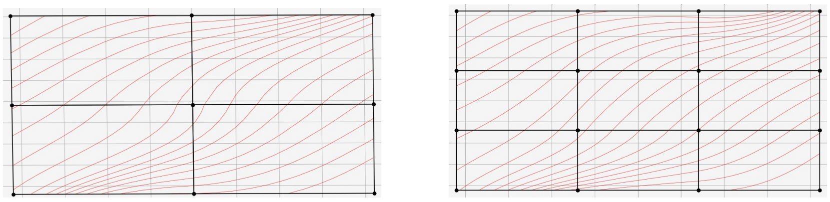

(a) with a 2 by 2 mesh

(b) with a 3 by 3 mesh

Figure 5.7: Fibre tow paths as obtained by maximizing the buckling load

Figure 5.7 displays the results of optimizing the tow paths for the buckling load case by the software developed in this thesis, while Figure 5.6 shows the fibre directions in the CM mesh for an optimal ply layup as found by [1]. Both of these are showing an S shaped tow path.

5.3 3 dimensional tension

As a final test the 3 dimensional capabilities of the program are verified by loading a single curved structure in tensile. The MM on this curved structure is as shown in Figure 5.8. The tensile load is in the y-direction while the fibre angle 0^o is orientated parallel to the x-axis.

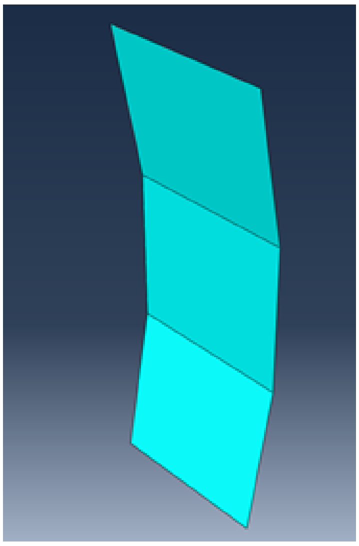

Figure 5.8: The manufacturing mesh elements used to represent a curved plate

In Table 5.3 the results of the optimization procedure for different starting plies are shown. In the panels that have been optimized to maximize the tensile failure the fibres are oriented in the direction of the tensile load as expected. The results are mapped with a tow-path planner and are shown in Figure 5.9.

Table 5.3: Optimized layup for the 3D tensile load case with different starting layups

	Starting layup	Optimized layup
Case 1	[0]	[89.93]
Case 2	[45]	[89.98]
Case 3	[90]	[90]
Case 4	[-45]	[90]

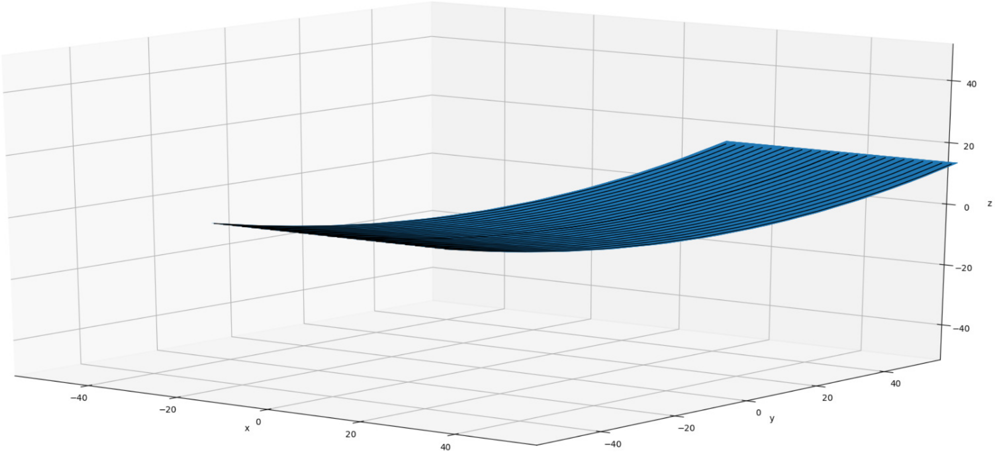

Figure 5.9: The tow paths on the curved plate after optimizing for maximum tensile load

Chapter 6

The density function

The density function is a continuous function based on the discretized fibre angles on the nodes of the manufacturing mesh (MM). The density function takes in account the variation of the ply stiffness properties caused by gaps and overlaps. It does this based on the discrete fibre angles in the MM. In section 6.1 first the already existing 2D approach to this problem is reviewed and how the density function can be moved to a 3 dimensional geometry is discussed. In section 6.2 some of the complications are discussed and an alternative solution is proposed, which is compared against some of the results found by other researchers.

6.1 Density function

When fibre steering, overlaps and gaps are created. To address the effects of these defects, the stiffness can be corrected using the increased or reduced density caused by a overlap and gap respectively.

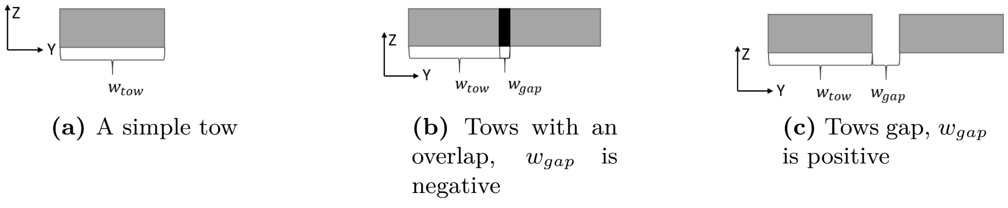

(a) A simple tow

(b) Tows with an overlap, w_{gap} is negative

(c) Tows gap, w_{gap} is positive

Figure 6.1: Tow cross-sections, shown normal to the fibre.

Using Figure 6.1 a new value for the thickness of the tow can be defined. The local thickness of the tow is defined in such fashion that it is equal to the tow area divided by the sum of the gap width and the tow width.

The solution to finding the density at a location (x, y) is found using a approximate numerical method. Three different possible methods are available:

1. Functional approximation method
2. Finite difference method
3. Finite element method

Both the functional approximation method and the finite difference method require the use of the boundary conditions as defined in the main problem. To solve find a expression for the density as a function of the fibre angle, a continuous function is assumed. First a fictional tow height is found based on gap or overlaps size.

$$h_{loc}\left(w_{tow}+w_{gap}\right)=h_{tow}\left(w_{tow}+w_{gap}\right)-h_{tow}w_{gap} \tag{6.1}$$

For an overlap the local thickness can be found using Eq. (6.1). The width of the gap w_{gap} as defined in the equation is negative for an overlap.This reduces Eq. (6.1) to Eq. (6.2). In this equation h_{loc} signifies a local average height of a fibre, taking in account the gap or overlap.

$$h_{loc}=h_{tow}\frac{w_{tow}}{w_{gap}+w_{tow}} \tag{6.2}$$

For a gap the local thickness can be found using Eq. (6.3).

$$h_{loc}\left(w_{tow}+w_{gap}\right)=h_{tow}\left(w_{tow}+w_{gap}\right)+h_{gap}w_{gap} \tag{6.3}$$

In Eq. (6.3) the height of the tow at the gap (h_{gap}) is 0. Thus the equation for the local thickness at a gap can be re-written to Eq. (6.2). In this equation the width of the gap is a function of x and y. Thus the equation becomes the following:

$$h_{loc}=h_{tow}\frac{w_{tow}}{w_{gap}\left(x,y\right)+w_{tow}} \tag{6.4}$$

Adjusting the thickness locally would also impact the geometry of the ply and would invalidate the classical laminated plate theory (CLPT), as the Kirchoff-Love plate theory (KLPT) would no longer hold. The KLPT requires the mid-surface to be a plane. This is not true if the thickness of the plate is not constant. So instead the local tow thickness is replaced by a fictitious density function. The fictitious density is defined by Eq. (6.5), where ρ^k_{fict} is used to symbolize the fictional density in ply k.

$$\rho_{fict}=\frac{w_{tow}}{w_{gap}\left(x,y\right)+w_{tow}} \tag{6.5}$$

This alternative does not violate the KLPT assumptions. Now the laminate stiffness matrices can be rewritten as:

$$A_{ij}=\sum_{k=1}^{n}\rho^k_{fict}\left[\bar{Q}_{ij}\right]_k\left(z_{k+1}-z_k\right) \tag{6.6}$$

$$B_{ij} = \sum_{k=1}^{n} \rho^k_{fict} \left[\bar{Q}_{ij}\right]_k \left(z^2_{k+1} - z^2_k\right) \tag{6.7}$$

$$D_{ij} = \sum_{k=1}^{n} \rho^k_{fict} \left[\bar{Q}_{ij}\right]_k \left(z^3_{k+1} - z^3_k\right) \tag{6.8}$$

The density function is assumed to a continuous function of the form of Eq. (6.9)

$$\rho^{e,k}(x,y) = \rho^k_0 + \rho^{e,k}_m(x,y) + \int_{x_0}^{x} \frac{\partial \rho^{e,k}}{\partial x} dx + \int_{y_0}^{y} \frac{\partial \rho^{e,k}}{\partial y} dy \tag{6.9}$$

The density function is differently defined in each element and ply, denoted by e and k respectively. x and y denote the coordinates within the element. The density ρ_0 is a reference point where the density is known. The term $\rho^{e,k}_m(x,y)$ is used to change the distance between the starting point of two tows during the lay-up process. Depending on the lay-up strategy the distance between tows may be increased or decreased.

The term $\rho^{e,k}_m(x,y)$ is found using the Lagrangian interpolation. The correction terms are defined to be on the nodes of the MM. To find the correction in the calculation mesh (CM) elements the same method is used as the method to find the fibre angles in the CM elements as described in 3.4.

$$\rho^{e,k}_m(x,y) = -\sum_{i=1}^{4} N_i \cdot \chi^{e,k}_i \tag{6.10}$$

In Eq. (6.10) $\chi^{e,k}_i$ denotes the nodal correction terms on the MM as supplied by the engineer. If no correction is created by the engineer, these values should be set to 0. In Eq. (6.10) the N_i denotes the Lagrangian shape function as previously shown in Eq. (3.32) through Eq. (3.35).

From Eq. (6.9) the last two terms are used relate the change in the fibre angle ϕ to the change in density ρ. To do so visualizing the path of a tow with the direction s being tangent to the direction of the fibre and n is normal to the fibre, see Figure 6.2.

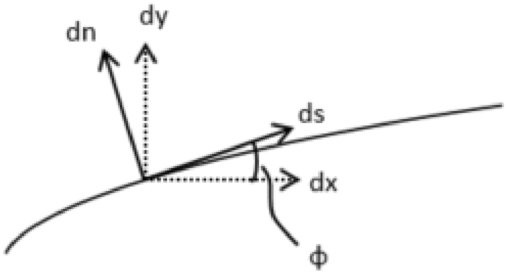

Figure 6.2: A fibre with the tangent and normal directions [4]

Eq. (6.11) describes an unknown relation between the fibre angle and the density.

$$\frac{\partial \rho}{\partial s} = f\left(\frac{\partial \phi}{\partial n}\right) \tag{6.11}$$

If the previous equation is describing a linear relation Eq. (6.12) can be assumed.

$$\frac{\partial \rho}{\partial s} = -k_c \frac{\partial \phi}{\partial n} \tag{6.12}$$

To be able to use this relation the fractions on the left and right hand side of Eq. (6.12) need to be functions of x and y. The change in fibre angle normal to the curve can be found in Eq. (6.13)

$$\frac{\partial \phi}{\partial n} = \frac{\partial \phi}{\partial x}\frac{\partial x}{\partial n} + \frac{\partial \phi}{\partial y}\frac{\partial y}{\partial n} \tag{6.13}$$

For the density Eq. (6.14) is valid.

$$\frac{\partial \rho}{\partial s} = \frac{\partial \rho}{\partial x}\frac{\partial x}{\partial s} + \frac{\partial \rho}{\partial y}\frac{\partial y}{\partial s} \tag{6.14}$$

Looking at Figure 6.2 the following relations can be found $\frac{\partial y}{\partial s} = \sin(\phi)$, $\frac{\partial x}{\partial s} = \cos(\phi)$, $\frac{\partial y}{\partial n} = \cos(\phi)$, and $\frac{\partial x}{\partial n} = -\sin(\phi)$. Substituting this into Eq. (6.13) and Eq. (6.14) results in the equations below.

$$\frac{\partial \phi}{\partial n} = -\frac{\partial \phi}{\partial x}\sin(\phi) + \frac{\partial \phi}{\partial y}\cos(\phi) \tag{6.15}$$

$$\frac{\partial \rho}{\partial s} = \frac{\partial \rho}{\partial x}\cos(\phi) + \frac{\partial \rho}{\partial y}\sin(\phi) \tag{6.16}$$

Substituting these in Eq. (6.12) results in Eq. (6.17)

$$\frac{\partial \rho}{\partial x}\cos(\phi) + \frac{\partial \rho}{\partial y}\sin(\phi) = k_c\frac{\partial \phi}{\partial x}\sin(\phi) - k_c\frac{\partial \phi}{\partial y}\cos(\phi) \tag{6.17}$$

Isolating the terms that don't interact results in Eq. (6.18)

$$\begin{aligned} \frac{\partial \rho}{\partial x} &= -k_c\frac{\partial \phi}{\partial y} \\ \frac{\partial \rho}{\partial y} &= k_c\frac{\partial \phi}{\partial x} \end{aligned} \tag{6.18}$$

Substituting this and Eq. (6.10) in the original equation, Eq. (6.9). Results in Eq. (6.19)

$$\rho^{e,k}(x,y) = -\sum_{i=1}^{4} N_i \cdot \chi_i^{e,k} - k_c\int_{x_0}^{x} \frac{\partial \phi^{e,k}}{\partial y}dx + k_c\int_{y_0}^{y} \frac{\partial \phi^{e,k}}{\partial x}dy \tag{6.19}$$

The fiber angles can be found using the Lagrangian interpolation as described in section 3.4 Eq. (3.32) through Eq. (3.35) with Eq. (3.27) can be used as the mapping process moves the problem into isoparametric space. The resulting equation is shown in Eq. (6.20).

$$\phi = \frac{1}{4}\left[(1-x)(1-y)\phi_1^e + (1+x)(1-y)\phi_2^e + (1+x)(1+y)\phi_3^e + (1-x)(1+y)\phi_4^e\right] \tag{6.20}$$

Taking the partial derivative of the Eq. (6.20) to x and y results in Eq. (6.21) and Eq. (6.22).

$$\frac{\partial \phi}{\partial x} = \frac{1}{4}\left[(-1+y)\phi_1^e + (1-y)\phi_2^e + (1+y)\phi_3^e + (-1-y)\phi_4^e\right] \tag{6.21}$$

$$\frac{\partial \phi}{\partial y} = \frac{1}{4}\left[(-1+x)\phi_1^e + (-1-x)\phi_2^e + (1+x)\phi_3^e + (1-x)\phi_4^e\right] \tag{6.22}$$

Substituting Eq. (6.21) and Eq. (6.22) into Eq. (6.19) results in Eq. (6.23)

$$\begin{aligned}
\rho^{e,k}(x,y) &= \rho_0 - \sum_{i=1}^{4} N_i \cdot \chi_i^{e,k} \\
-\frac{k_c}{4}\int_{x_0}^{x} &\left[(-1+x)\phi_1^e + (-1-x)\phi_2^e + (1+x)\phi_3^e + (1-x)\phi_4^e\right] dx \\
+\frac{k_c}{4}\int_{y_0}^{y} &\left[(-1+y)\phi_1^e + (1-y)\phi_2^e + (1+y)\phi_3^e + (-1-y)\phi_4^e\right] dy
\end{aligned} \tag{6.23}$$

Rewriting and integration Eq. (6.23):

$$\begin{aligned}
\rho^{e,k}(x,y) = \rho_0 &- \sum_{i=1}^{4} N_i \cdot \chi_i^{e,k} \\
&+\frac{k_c}{4}\left[\left(-\frac{1}{2}(x^2-x_0^2) + (x-x_0) + \frac{1}{2}(y^2-y_0^2) - (y-y_0)\right)\phi_1^e\right. \\
&+\left(\frac{1}{2}(x^2-x_0^2) + (x-x_0) - \frac{1}{2}(y^2-y_0^2) + (y-y_0)\right)\phi_2^e \\
&+\left(-\frac{1}{2}(x^2-x_0^2) - (x-x_0) + \frac{1}{2}(y^2-y_0^2) + (y-y_0)\right)\phi_3^e \\
&+\left.\left(\frac{1}{2}(x^2-x_0^2) - (x-x_0) - \frac{1}{2}(y^2-y_0^2) - (y-y_0)\right)\phi_4^e\right]
\end{aligned} \tag{6.24}$$

This allows for the implementation of the density function, which attempts to estimate the size gaps and overlaps in a fiber steered ply and the effect of those on the stiffness of the ply. This methodology is only applicable to a 2D environment. This can be moved into 3 dimensions using the same method as described in Chapter 3.

6.2 Complications of the density function

The density of a fibre steered ply dubbed the 'flower', of which the fibre angle distribution is as shown in Figure 6.3, is evaluated. The results are shown in Figure 6.4. On the line $y = -1$ the density is kept to 1, Diverging tows create gaps and thus a reduction in the density. The reduction in density is most extreme in the top corners, while on the line $x = 0$ the density remains 1. As there is no change in fibre angle along this line due to symmetry.

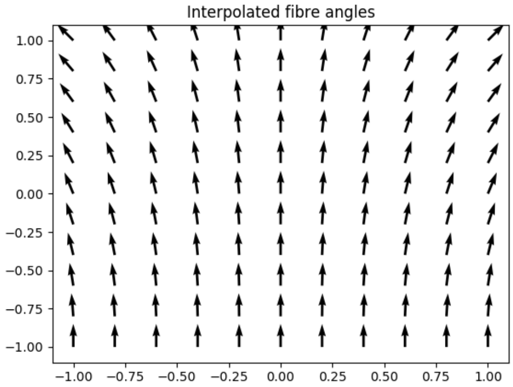

Figure 6.3: Fibre angle distribution for the 'flower'

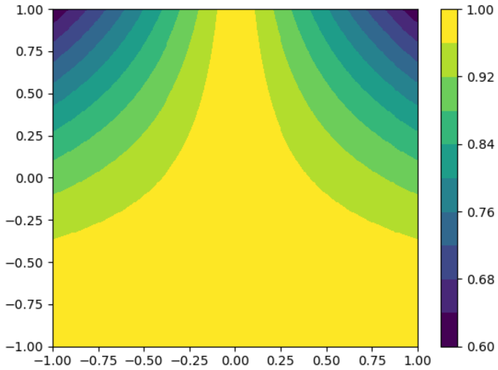

Figure 6.4: Density distribution for the 'flower'

The methodology works if the domain is simple geometry, like a rectangle as in the figure above, however when evaluating a *fatman* ply as shown in Figure 6.5(a) complications occur. The same procedure is used as before and the density along $y = 0$ is constant. When examining the top right quarter of the plate, the diverging angles create a boundary past which the plate contains no tows, unless an alternative iso-density line is defined for this second domain. The boundary shared by the two domains is shown in Figure 6.5(b), this phenomenon occurs in all four quarters of the plate for a total of 5 different domains.To take in account a boundary of which the shape changes each iteration is difficult.

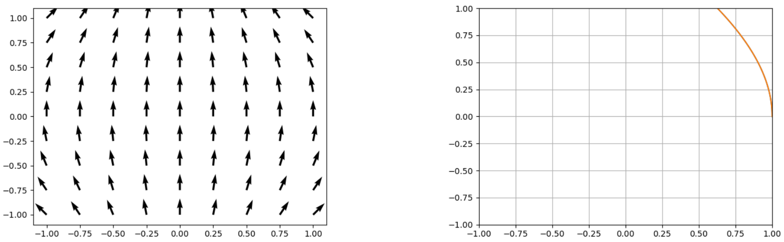

(a) Fibre angle distribution for the 'fatman'

(b) The streamline separating the two domains created in the top right quarter of the plate

Figure 6.5: Creation of two domains in the 'fatman'

To solve this problem the finite element method (FEM) is used instead, the first domain is given the same iso-density line along $y = 0$. The second domain is then populated with tows from the edge at $x = -1$ with another iso-density line along which the density is 1. To find the density first the change in the fibre angle has to be found for the top right quarter of the plate. The fibre angles in the nodes assuming the element covers a quarter of the plate are $90, 90, 135, 90$. The node numbering scheme is as shown in Figure 3.7. Figure 6.6(a) shows the fibre angle distribution over the element. The change in fibre angle is then expressed with respect to the fibre angle on the initial iso-density line $y = 0$, resulting in the following fibre angles in the nodes $0, 0, 45, 0$ as shown in Figure 6.6(b).

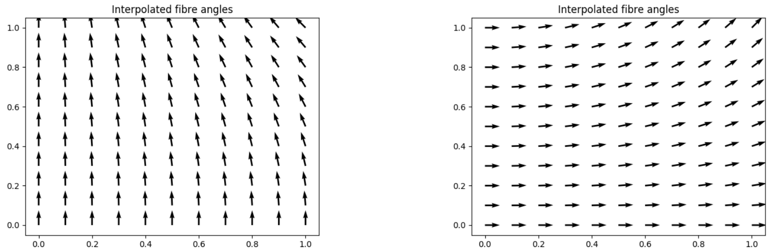

(a) The fibre angle on the top right quarter of the rectangular plate

(b) The change in fibre angle on the top right quarter of the rectangular plate

Figure 6.6: Distributions for a quarter of the rectangular plate

With FEM the sum of the change in fibre angle is considered to find the density. The fibre angle in the nodes is found using the Lagrangian interpolation function as shown in Eq. (6.25), with Eq. (6.26) as the shape functions.

$$d\phi(x, y) = \sum_{i=1}^{4} N_i(x, y) d\phi_i, \tag{6.25}$$

In this equation the N_i is the shape function where i represents the node with the node order as shown in Figure 3.7 and the x and y denote the coordinates where the change in fibre angle is desired.

$$\begin{aligned} N_1(\xi,\eta) &= \frac{1}{4ab}(x-x_2)(y-y_4), \qquad & N_2(\xi,\eta) &= -\frac{1}{4ab}(x-x_1)(y-y_3) \\ N_3(\xi,\eta) &= \frac{1}{4ab}(x-x_4)(y-y_2), \qquad & N_4(\xi,\eta) &= -\frac{1}{4ab}(x-x_3)(y-y_1) \end{aligned} \tag{6.26}$$

In this equation x and y denote the location at which the change the fibre angle is to be found, and the subscript is the node number. An example mesh is shown in Figure 6.7, the density of node 6 is found by adding the change in fibre angle to the density of the node below as illustrated by Eq. (6.27).

$$\rho_6 = \rho_1 + d\phi(x,y)_6 \tag{6.27}$$

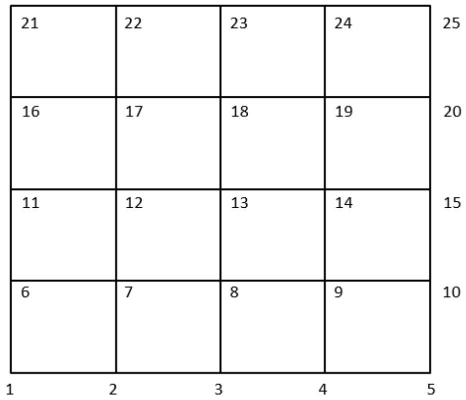

Figure 6.7: Example mesh to illustrate the procedure for finding the density.

Repeating this process with the iso-density line set at the line $x = 1$, while taking the sum from right to left instead of upwards results in Figure 6.8.

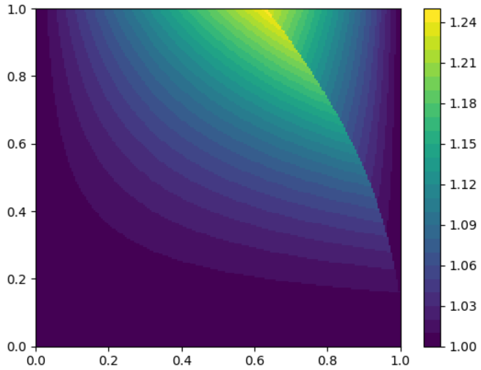

Figure 6.8: The density field for a quarter of the geometry using two iso-density lines at $y = 0$ and $x = -1$

Van Tooren et al. [6] show a density field based on the post tow path planning averaging as presented in Figure 6.9.

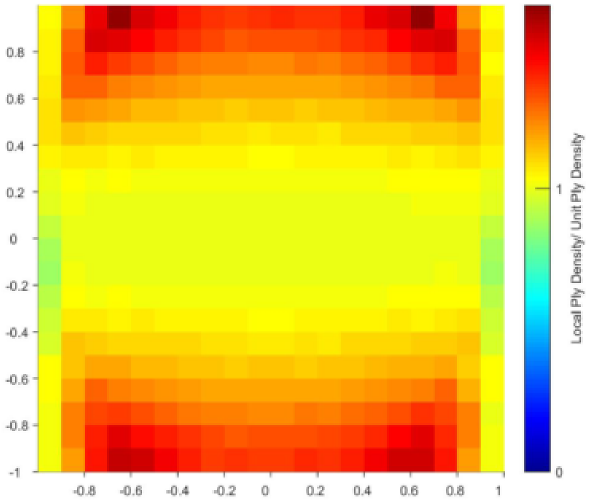

Figure 6.9: The density field of the 'fatman' based on a post tow path planning averaging [6]

Note that other strategies are available to dealing with the empty corners created when setting an iso-density line at $x = 0$. An example alternative strategy is to extend the original iso-density line past the plate until the tows, which originate from outside the plate, fill up the corners. The first strategy is shown in Figure 6.10(a) and the second in Figure 6.10(b). The density field that corresponds to the second manufacturing strategy is shown in Figure 6.11.

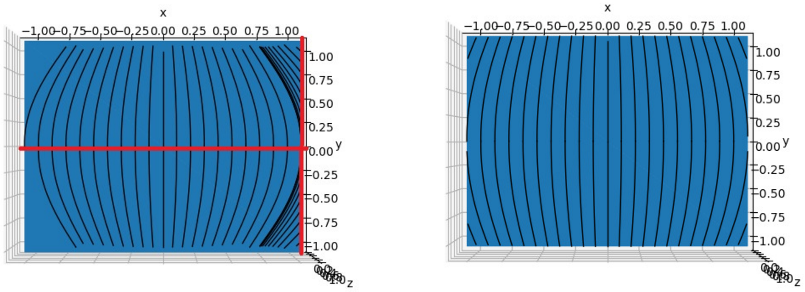

(a) Seed lines are as indicated by the red lines

(b) Seed line is on $y = 0$ and is of infinite length

Figure 6.10: The tows for the 'fatman' case with two different manufacturing approaches

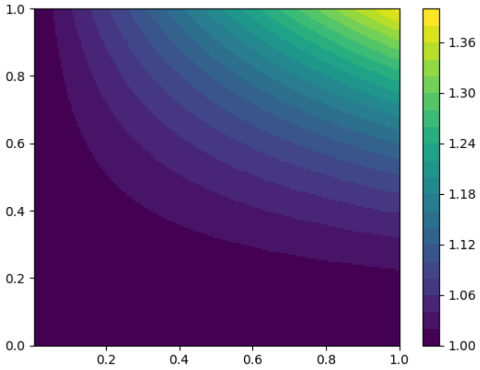

Figure 6.11: The density field based using a singular iso-density line of infinite length

This highlights the effect of the manufacturing strategy on the density field. The amount of overlap Figure 6.8 is significantly less in Figure 6.11, this difference is dependent on the manufacturing strategy and the fibre angle distribution. The manufacturing strategy depends on how the fibre angles in the ply are distributed. The first manufacturing strategy as shown in Figure 6.10(a) generates a shock wave, akin to the shock waves generated in compressible flow problems. These indicate discontinuous changes. This problem is not limited to the fatman case, it also occurs when optimizing for maximum buckling load. For the S-shaped fibre distribution the iso-density line is on the edges $y = -100$ and $x = -100$ of the square plate a shock wave is created as demonstrated in Figure 6.12.

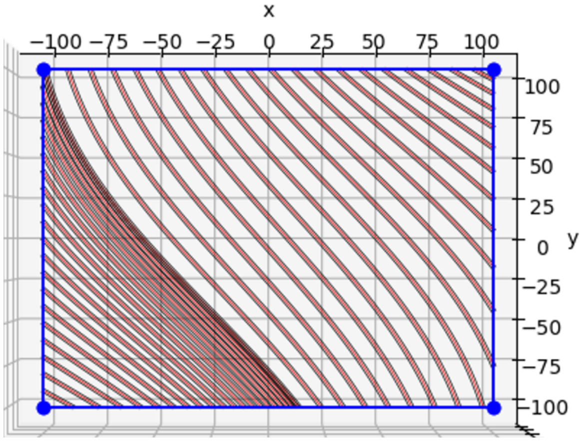

Figure 6.12: A shock wave as created during optimization for maximum buckling load

To relate this to a curved panel is possible through the same methodology as discussed in Chapter 3. To recap; the MM element is rotated in a single plane, then the element is mapped into the natural coordinate system. After this process the FEM approach described above can find a correction factor for the stiffness of the material.

6.3 Conclusion

The interdependency of the manufacturing strategy and the fibre angle distribution create a complex problem. To solve this problem additional research is required to determine a manufacturing strategy sufficient to cover the geometry with tows. The current implementation assumes that the automated fibre placement (AFP) machine starts from the middle of the plate when laying the tows. As shown in Figures 6.11 and 6.8, this is not the optimal manufacturing strategy and only evaluating the fibre angle distribution using this simple manufacturing strategy is simplifying the problem inappropriately.

Chapter 7

Conclusion

7.1 Conclusion

The objective of the manuscript was to find a methodology that could be used in combination with finite element analysis (FEA) to assess the effect of gaps and overlaps on the stiffness of fibre steered 3 dimensional geometry. In Chapter 2 an efficient methodology to optimize a fibre steered laminate for strength is identified. This method is known as the multiple mesh optimization approach (MMOA), which employs two different meshes. The first is a coarse mesh, named the manufacturing mesh (MM). In the nodes of this mesh the design variables (fibre angles) are defined. From this mesh the fibre angles are interpolated on the second mesh, coined the calculation mesh (CM). This fine mesh, with the fibre angles in its elements, is imported into ABAQUS® to be used for the evaluation.

Through a process of rotation and mapping of the MM elements into iso-parametric space the MMOA is modified to allow for the evaluation of 3 dimensional geometries. The process to achieve this is elaborated upon in Chapter 3. The implementation of this process in code is discussed in Chapter 4. In Chapter 5 the implementation is verified by comparing the results for various standard cases, such as a tensile and buckling case, with the results obtained by researchers previously active in the field. The comparison in this chapter validates the results of the optimization, this is mostly done through 2 dimensional cases as there is currently no literature available for fibre steering on 3 dimensional surfaces.

The density function is introduced and the validity of the density function is evaluated. Domains are created for which different manufacturing strategies are feasible; these influence the distribution and severity of the gaps and overlaps. A general solution for the cases presented is extending the initial iso-density line until the plate is filled, however this causes larger gaps and overlaps than other manufacturing strategies.

7.2 Recommendations

A general method that averts the creation of multiple domains, while not creating an excessive amount of gaps and overlaps. A possible solution is to create the iso-density in the form of a spline instead of a straight line. Placing that spline based on the fibre angles in the nodes of the MM. This spline would be within the bounds of the geometry, thus creating less gaps and overlaps than extending a hypothetical line.

Alternatively XFEM can be used to deal with the discontinuities in the density function. As for XFEM the finite element mesh does not have to be adapted based on boundaries of the domain that is generated when creating multiple iso-density lines.

In the current evaluation for the density correction factor the iso-density line is defined as 1, indicating that the line contains no gaps or overlaps. This does not have to be the best solution, as creating slight overlaps or gaps in the iso-density line can result in a better solution depending on the evaluation criteria.

A different optimization algorithm; more suited for the problem should be found and implemented. SLSQP linearizes the problem space created by the cost function. The solution space is very "spikey" due to the fact that a single change the design variable changes the whole stress field, and from this stress field only the maximum stress is returned.

To get a closer to realistic estimation of the failure, a different failure criteria can be implemented. The current Tsai-Wu criteria does not take in account stresses in individual plies or edge stresses that are generated through-out a fibre steered ply. A possible avenue of improving the methodology is to look into implementing the LaRC05 or Puck failure stress criteria, which take into account different failure modes instead of trying to approximate failure through a single formula. Another avenue of improvement is to implement progressive damage analysis in the optimization procedure.

A final suggestion is to use a global interpolation method instead of a mesh based interpolation method for the fibre angles. This will solve the problem of limited continuity as would be with Lagrangian interpolation functions. Examples of two ways this can be achieved is through non-uniform rational basis spline (NURBS) or radial basis functions (RBF), if local interpolation functions can not be deviated from a different shape function such as Bézier curves or Hermite interpolation functions.

References

[1] Darun Barazanchy. A new framework for optimization of variable stiffness plates. *58th AIAA/ASCE/AHS/ASC Structures, Structural Dynamics, and Materials Conference*, 2017.

[2] Adriana W. Blom, Claudio S. Lopes, Peter J. Kromwijk, Zafer Gürdal, and P. P. Camanho. A theoretical model to study the influence of tow-drop areas on the stiffness and strength of variable-stiffness laminates. *Journal of Composite Materials*, 43(5):403–425, 2009.

[3] Kazem Fayazbakhsh. *The impact of gaps and overlaps on variable stiffness composites manufactured by Automated Fiber Placement.* McGill University, 2013.

[4] Michel J. Van Tooren, David Lucas, and Ali Elham. Stiffness Corrections for Overlaps and Gaps in Steered Composite Panel Optimization. *58th AIAA/ASCE/AHS/ASC Structures, Structural Dynamics, and Materials Conference*, 2017.

[5] Chongyu Hua. An inverse transformation for quadrilateral isoparametric elements: Analysis and application. *Finite Elements in Analysis and Design*, 7(2):159–166, 1990.

[6] Michel J L van Tooren, David A Lucas, Luis G Bahamonde Jácome, Ifat Jahangir, Darun Barazanchy, and Ali Elham. Rapid Quantification of Gaps and Overlaps for Fiber Steering Design Optimization. *AIAA/ASCE/AHS/ASC Structures, Structural Dynamics, and Materials Conference*, 2018.

[7] B. F.Tatting and Z. Guerdal. Design and Manufacture of Elastically Tailored Tow Placed Plates. *Nasa archive*, 2002.

[8] Shahriar Setoodeh, Mostafa M. Abdalla, and Zafer Gürdal. Design of variable-stiffness laminates using lamination parameters. *Composites Part B: Engineering*, 37(4-5):301–309, 2006.

[9] Michel van Tooren, Ali Elham, R Harik, and Darun Barazanchy. Design of variable stiffness composite plates with cut-outs using a dual mesh approach. *16th AIAA/ISSMO Multidisciplinary Analysis and Optimization Conference*, 09 2015.

[10] H.T. Hahn and S.W. Tsai. *Introduction to Composite Materials.* Taylor & Francis, 1980.

[11] Stephen W Tsai and Nicholas J Pagano. *Invariant properties of composite materials.* Technomic Pub. Co., Stamford, CT, 1968.

[12] Mitsunori Miki and Yoshihiko Sugiyamat. Optimum Design of Laminated Composite Plates Using Lamination Parameters. *AIAA Journal*, 31(5):921–922, 1993.

[13] J. Foldager, J. S. Hansen, and N. Olhoff. A general approach forcing convexity of ply angle optimization in composite laminates. *Structural Optimization*, 16(2-3):201–211, 1998.

[14] S. T. Ijsselmuiden, M. M. Abdalla, and Z. Gürdal. Implementation of Strength-Based Failure Criteria in the Lamination Parameter Design Space. *AIAA Journal*, 46(7):1826–1834, jul 2008.

[15] A. Khani, S. T. Ijsselmuiden, M. M. Abdalla, and Z. Gürdal. Design of variable stiffness panels for maximum strength using lamination parameters. *Composites Part B: Engineering*, 42(3):546–552, 2011.

[16] Daniël M.J. Peeters, Gustavo Gonzalez Lozano, and Mostafa M. Abdalla. Effect of steering limit constraints on the performance of variable stiffness laminates. *Computers and Structures*, 196:94–111, 2018.

[17] C. S. Lopes. *Damage and Failure of Non-Conventional Composite Laminates.* Delft University of Technology, 2009.

[18] M Arian Nik, K Fayazbakhsh, D Pasini, and L Lessard. The effect of gaps and overlaps on the in-plane stiffness and buckling load of variable stiffness laminates made by automated fiber placement. *15th European Conference on Composite Materials*, 2012.

[19] I.C. Taig. *Structural Analysis by the Matrix Displacement Method.* English Electric Aviation Report, 1961.

[20] Jorge Nocedal. *Numerical optimization.* Springer, New York, 2006.

[21] J. N. Reddy. *Mechanics of laminated composite plates and shells : theory and analysis.* CRC Press, Boca Raton, 2004.

[22] M. Walker, S. Adali, and V. Verijenko. Optimization of symmetric laminates for maximum buckling load including the effects of bending twisting coupling. *Computers and Structures*, 58(2):313–319, 1996.

[23] Shahriar Setoodeh, Mostafa M. Abdalla, Samuel T. IJsselmuiden, and Zafer Gürdal. Design of variable-stiffness composite panels for maximum buckling load. *Composite Structures*, 87(1):109–117, 2009.

[24] Daniël M.J. Peeters, Simon Hesse, and Mostafa M. Abdalla. Stacking sequence optimisation of variable stiffness laminates with manufacturing constraints. *Composite Structures*, 125:596–604, 2015.

Appendix A

Building rotation matrix through changing basis

A.1 Building rotation matrix through changing basis

Given that the unit vector normal to the xy-plane is $[0, 0, 1]$ denoted as $\boldsymbol{m}$, a rotation matrix to rotate the manufacturing mesh (MM) element and its calculation mesh (CM) centroids can be found. To do so, realize that the rotation is going to be around and unknown axis p and by and unknown rotation angle θ. The rotation is a 2D rotation around $\boldsymbol{p}$. The rotation matrix for a 2D rotation is given by Eq. (A.1)

$$\boldsymbol{R_{2D}} = \begin{bmatrix} \cos(\theta) & -\sin(\theta) & 0 \\ \sin(\theta) & \cos(\theta) & 0 \\ 0 & 0 & 1 \end{bmatrix} \tag{A.1}$$

This is true in a hypothetical basis with $\boldsymbol{p}$ as its third axis. The axis of rotation is orthogonal to both the unit normal vector of the MM element $\boldsymbol{n}$ and unit vector $\boldsymbol{m}$. Thus the third axis can be described by Eq. (A.2).

$$\boldsymbol{r} = \boldsymbol{n} \otimes \boldsymbol{m} \tag{A.2}$$

Now we need to create the remaining 2 axis that are orthogonal in the plane of vectors $\boldsymbol{n}$ and $\boldsymbol{m}$. Two vectors in one plane that are orthogonal are the projection of one vector on the other and the rejection of that same vector on the other. So the first axis will be the normalized projection of $\boldsymbol{m}$ on $\boldsymbol{n}$ as described by $\boldsymbol{m_p}$ in Figure A.1.

Since both $\boldsymbol{m}$ and $\boldsymbol{n}$ are unit vectors and the basis is to be orthonormal the first axis of the orthonormal basis can be found using Eq. (A.3).

$$\boldsymbol{m_p} = \frac{(\boldsymbol{m} \cdot \boldsymbol{n})\boldsymbol{n}}{|\boldsymbol{n}|^2} \tag{A.3}$$

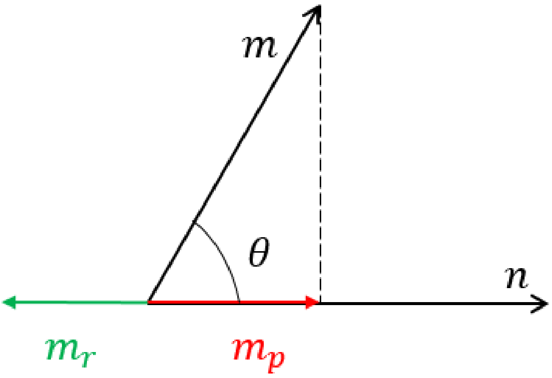

Figure A.1: Vector projection of $\boldsymbol{m}$ onto $\boldsymbol{n}$ in red, vector rejection of $\boldsymbol{m}$ onto $\boldsymbol{n}$ in green.

Now given that n is a normalized vector and has a length of 1 the $|\boldsymbol{n}|^2$ term can be neglected. Normalizing the projection of $\boldsymbol{m}$ on $\boldsymbol{n}$ results in Eq. (A.4).

$$\boldsymbol{p} = \frac{\boldsymbol{m_p}}{|\boldsymbol{m_p}|} = \frac{(\boldsymbol{m}\cdot\boldsymbol{n})\boldsymbol{n}}{(|\boldsymbol{m}\cdot\boldsymbol{n})\boldsymbol{n}|} = \boldsymbol{n} \tag{A.4}$$

So the first axis of the orthonormal basis is $\boldsymbol{n}$.

Finally the vector describing the second axis has to be orthogonal to the first and third axis. This is the normalized vector rejection of $\boldsymbol{m}$ on $\boldsymbol{n}$ as shown in Figure A.1, as this vector lies in the plane of the vectors $\boldsymbol{n}$ and $\boldsymbol{m}$ while being orthogonal to vector $\boldsymbol{n}$. This vector is mathematically described by Eq. (A.5), where $\boldsymbol{m_p}$ is the vector projection of $\boldsymbol{m}$ onto $\boldsymbol{n}$.

$$\boldsymbol{q} = \frac{\boldsymbol{m}-\boldsymbol{m_p}}{||\boldsymbol{m}-\boldsymbol{m_p}||} \tag{A.5}$$

Given that the projection of $\boldsymbol{m}$ on $\boldsymbol{n}$ is $(\boldsymbol{m}\cdot\boldsymbol{n})\boldsymbol{m}$, the vector rejection of $\boldsymbol{m}$ on $\boldsymbol{n}$ then becomes as described in Eq. (A.6)

$$\boldsymbol{q} = \frac{\boldsymbol{m}-(\boldsymbol{m}\cdot\boldsymbol{n})\boldsymbol{m}}{||\boldsymbol{m}-(\boldsymbol{m}\cdot\boldsymbol{n})\boldsymbol{m}||} \tag{A.6}$$

With $\boldsymbol{m}$ and $\boldsymbol{n}$ being unit vectors Eq. (A.1) can be rewritten to Eq. (A.7)

$$\boldsymbol{R_{2D}} = \begin{bmatrix} \boldsymbol{m}\cdot\boldsymbol{n} & -||\boldsymbol{m}\otimes\boldsymbol{n}|| & 0 \\ ||\boldsymbol{m}\otimes\boldsymbol{n}|| & \boldsymbol{m}\cdot\boldsymbol{n} & 0 \\ 0 & 0 & 1 \end{bmatrix} \tag{A.7}$$

The basis change matrix for basis of the rotation matrix $\boldsymbol{R_{2D}}$ is shown in Eq. (A.8)

$$\boldsymbol{H} = (\boldsymbol{p} \quad \boldsymbol{q} \quad \boldsymbol{r})^{-1} = \left(\boldsymbol{n} \quad \frac{\boldsymbol{m}-(\boldsymbol{m}\cdot\boldsymbol{n})\boldsymbol{m}}{||\boldsymbol{m}-(\boldsymbol{m}\cdot\boldsymbol{n})\boldsymbol{m}||} \quad \boldsymbol{n}\otimes\boldsymbol{m}\right)^{-1} \tag{A.8}$$

The final rotation matrix can be found by changing the basis as described in Eq. (A.9)

$$\boldsymbol{U} = \boldsymbol{H^{-1}R_{2D}H} \tag{A.9}$$

Now the rotation matrix $\boldsymbol{U}$ can be used to acquire the rotated MM element and CM centroids using Eq. (A.10)

$$\boldsymbol{v_{rot}} = \boldsymbol{Uv} \tag{A.10}$$

Where $\boldsymbol{v}$ is the point to be rotated into the xy-plane and $\boldsymbol{v_{rot}}$ is the rotated point in the xy-plane.

Appendix B

Validation of the centroid finding algorithm

To ensure the validity of the approach differently shaped quadrilateral elements are evaluated in this appendix. The elements chosen have centroid which can be found through alternate means. The first element is a simple 2 dimensional rectangular element. The node coordinates of this element are shown in Table B.1. The element and its centroid are displayed in Figure B.1.

Table B.1: Coordinates of the nodes of the 2D square

	x	y	z
node 1	0	0	0
node 2	1	0	0
node 3	1	1	0
node 4	0	1	0

The element is a simple rectangle with sides of length 1 so the centroid is located in the middle of the rectangular element at $[0.5, 0.5, 0]$. The proposed methodology finds the centroid to be located at $[0.5, 0.5, 0]$.

To check how the function works with a heavily deformed element, a triangle is evaluated. The nodes of the triangle are given in Table B.2

Table B.2: Coordinates of the nodes of the 2D wedge

	x	y	z
node 1	0	0	0
node 2	1	0	0
node 3	0.5	1	1
node 4	0.5	1	1

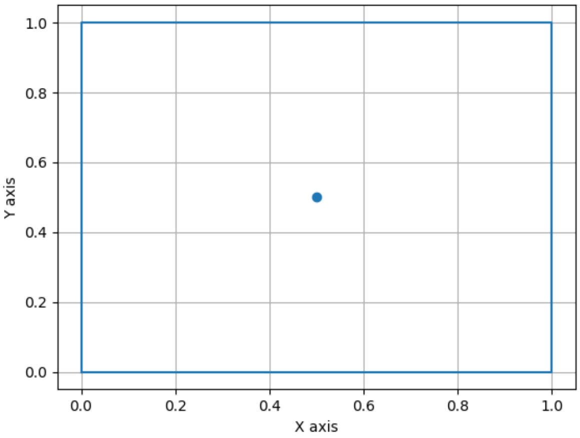

Figure B.1: A 2D square surface with its centroid

The methodology finds that the centroid should be located at $[0.5, 0.333, 0]$. Using the formula of the centroid of a triangle 3.1, the same location is found for the centroid.

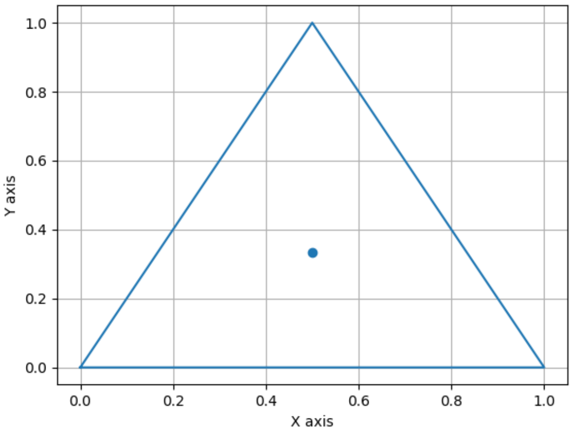

Figure B.2: A 2D wedge surface with its centroid

Appendix C

Validation of the conditions of the inverse iso-parametric mapping procedure

Condition 1: $a_1 = 0$, $a_2 = 0$ For this condition the element is a square in the global coordinate system. To verify an example with the nodes as shown in Table C.1

Table C.1: Node coordinates for first condition

	x	y	z
node 1	0	0	0
node 2	1	0	0
node 3	1	1	0
node 4	0	1	0

The point of which the natural coordinates need to be found is $[0.5, 0.5]$. Transforming to the natural coordinate system results in $[0, 0]$ so for this condition the transformation is correct.

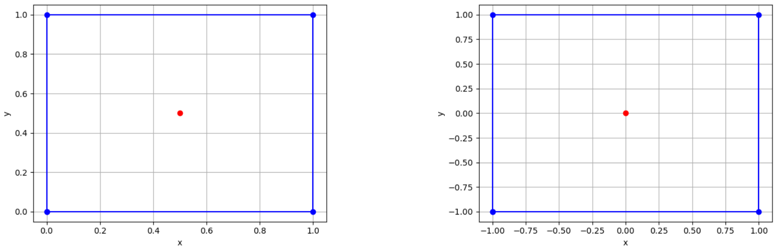

(a) fig:case1before **(b)** fig:case1after

Figure C.1: The quadrilateral element before and after transformation for the first condition

Condition 2: $a_1 = 0$, $a_2 \neq 0$, $c_1 = 0$ For this condition $(x_1 + x_3) - (x_2 + x_4) = 0$ however $(y_1 + y_3) - (y_2 + y_4) = 0$ this is not true. While the condition $c_1 = 0$ means that $(x_3 + x_4) - (x_1 + x_2) = 0$. The result is an element as given in Table C.2.

Table C.2: Node coordinates for second condition

	x	y	z
node 1	0	0.5	0
node 2	1	0	0
node 3	1	1	0
node 4	0	1	0

The average of the nodes is found to be at $[0.5, 0.625]$ which after the transformation to the iso-parametric space results in $[0, 0]$ as is shown in Figure C.2.

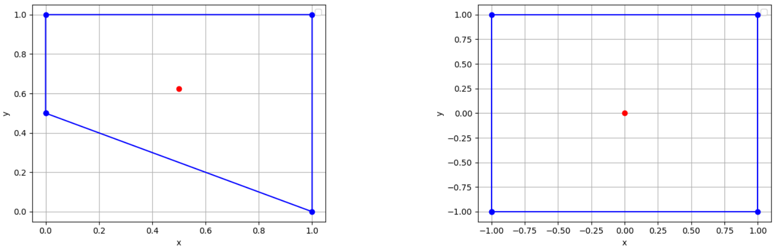

(a) fig:

(b) fig:

Figure C.2: The quadrilateral element before and after transformation for the second condition

Condition 3: $a_1 = 0$, $a_2 \neq 0$, $c_1 \neq 0$ Then using Eq. (3.21). Now c_1 is not equal to 0, $(x_3 + x_4) - (x_1 + x_2) \neq 0$ while $(x_1 + x_3) - (x_2 + x_4) = 0$. An element that fulfills these conditions is shown in Table C.3. The average sum of the nodes is $[0.75, 0.65]$.

Table C.3: Node coordinates for third condition

	x	y	z
node 1	0.5	0	0
node 2	1	1	0
node 3	1	1.1	0
node 4	0.5	0.5	0

After the transformation to the natural coordinate system the result is found to be in $[0, 0]$. As shown in Figure C.3.

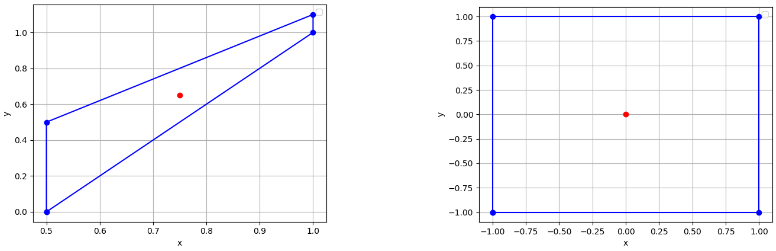

(a) fig: **(b)** fig:

Figure C.3: The quadrilateral element before and after transformation for the third condition

Condition 4: $a_1 \neq 0$, $a_2 \neq 0$, a_b & $a_c \neq 0$ For this condition using Eq. (3.22). The natural coordinates can be found of the mid point of the 4 nodes. The element that is adhering to these conditions is as shown in Table C.4. The node average is at $[0.625, 0.675]$, which after transformation to the natural coordinate system results in $[0, 0]$ as expected. The result is shown in Figure C.4

Table C.4: Node coordinates for fourth condition

	x	y	z
node 1	0	0	0
node 2	1	0	0
node 3	1.5	1.5	0
node 4	0	1.2	0

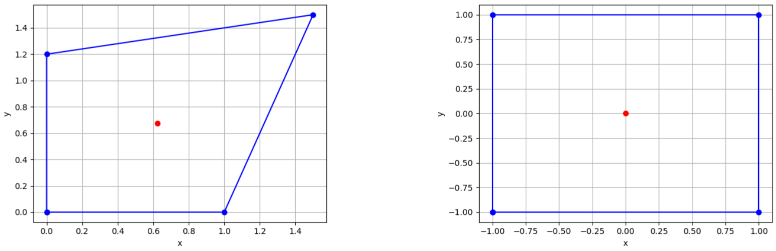

(a) fig: **(b)** fig:

Figure C.4: The quadrilateral element before and after transformation for the fourth condition

Condition 5: $a_1 \neq 0$, $a_2 \neq 0$, $a_b \neq 0$ & $a_c = 0$ In this case an element that fulfills this condition is shown in Table C.5. The average of the nodes is located at $[0.625, 0.375]$, as expected and shown in Figure C.5 the average of the nodes is mapped to $[0, 0]$.

Table C.5: Node coordinates for fifth condition

	x	y	z
node 1	0	0	0
node 2	1	0	0
node 3	1.5	1.5	0
node 4	0	0	0

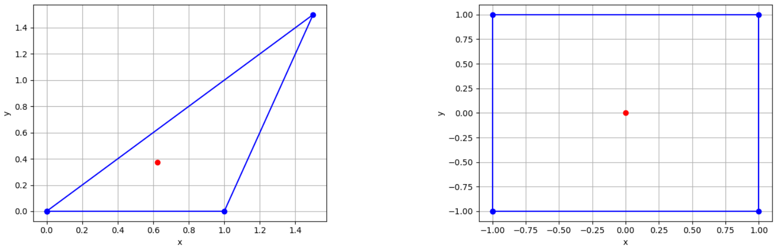

(a) fig: **(b)** fig:

Figure C.5: The quadrilateral element before and after transformation for the fifth condition

Condition 6: $a_1 \neq 0$, $a_2 \neq 0$, $a_b = 0$ & $a_c \neq 0$ For the sixth case the coordinates of the nodes of the quadrilateral element are as displayed in Table C.6.

Table C.6: Node coordinates for sixth condition

	x	y	z
node 1	0	0	0
node 2	1	0.5	0
node 3	1.5	1.5	0
node 4	0	0.75	0

The element before and after transforming is shown in C.6. The average of the nodes before the transformation is $[0.625, 0.6875]$, after the transformation the average of the nodes is $[0, 0]$ as expected.

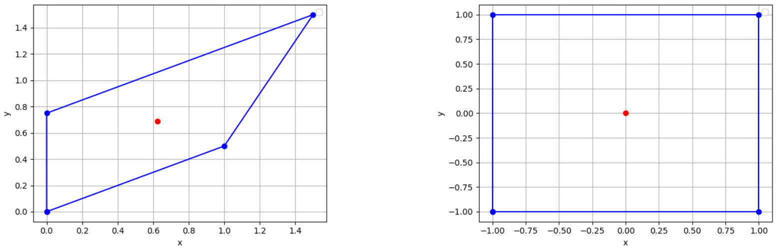

(a) fig: **(b)** fig:

Figure C.6: The quadrilateral element before and after transformation for the sixth condition

Condition 7: $a_1 \neq 0$, $a_2 = 0$ and $b_2 = 0$ In the seventh condition the fact that a_2 and b_2 have to be equal to 0 allow the element to be very close to a simple square element as can be seen in Figure C.7. The node locations for the original element are shown in Table C.7.

Table C.7: Node coordinates for seventh condition

	x	y	z
node 1	0	0	0
node 2	1	0	0
node 3	1.5	1.5	0
node 4	0	1.5	0

The average centroid before transformation is located in $[0.625, 0.75]$

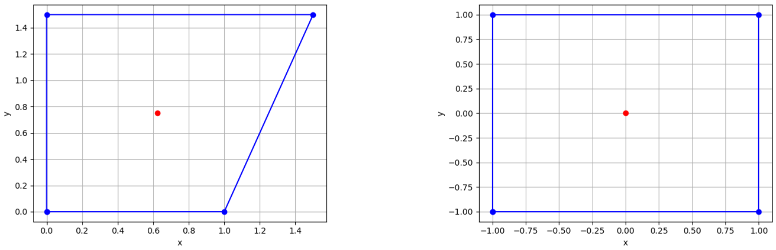

(a) fig: **(b)** fig:

Figure C.7: The quadrilateral element before and after transformation for the seventh condition

Condition 8: $a_1 \neq 0$, $a_2 = 0$ and $b_2 \neq 0$ For the final condition the nodes are as can be seen in Table C.8. The average centroid before transformation is located in $[0.375, 0.75]$.

The before and after images of the element can be seen in Figure C.8.

Table C.8: Node coordinates for eighth condition

	x	y	z
node 1	0	0.5	0
node 2	1	0	0
node 3	1	1	0
node 4	-0.5	1.5	0

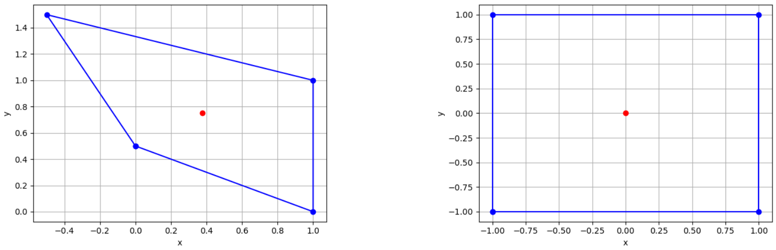

(a) fig:

(b) fig:

Figure C.8: The quadrilateral element before and after transformation for the last condition